# Atomic Force Microscopy and Nanomechanics of Bacteriophage T7

**Ph.D. Thesis**

## Zsuzsanna Vörös

Basic Medicine Doctoral School

Semmelweis University



| | |
|---|---|
| Supervisor: | Dr. Miklós Kellermayer MD, D.Sc |
| Official reviewers: | Dr. Csaba Dobó-Nagy MD, D.Sc. |
| | Dr. Attila Gergely Végh, Ph.D. |
| Final Examination Committee: | Dr. Emil Monos MD, D.Sc. (Chairman) |
| | Dr. Alán Alpár MD, Ph.D |
| | Dr. Beáta Bugyi, Ph.D |

Budapest

2018

TABLE OF CONTENTS

## ABBREVIATIONS

| | |
|---|---|
| **AFM** | Atomic Force Microscope |
| **APTES** | (3-Aminopropyl)triethoxysilane |
| **AP-mica** | Mica functionalized with APTES |
| **ATP** | Adenosine triphosphate |
| **CD** | Circular dichroism |
| **Cryo-EM** | Cryo-electron microscopy |
| **DNA** | Deoxyribonucleic acid |
| **dsDNA** | Double-stranded deoxyribonucleic acid |
| **EM** | Electron microscopy |
| **GD-mica** | Mica functionalized with glutaraldehyde |
| **gp** | Gene product |
| **OD** | Optical density |
| **PBS** | Phosphate-buffered saline |
| **RT** | Room temperature |
| **SD** | Standard deviation |
| **SPM** | Scanning Probe Microscope |
| **Tris** | tris(hydroxymethyl)aminomethane |

# 1 INTRODUCTION

Viruses are infectious obligate intracellular parasites that comprise a nanometer-sized protein shell (capsid) and an internal genome. The capsid protects the genome from exposure to harmful chemical and physical effects in the extracellular environment. In DNA viruses, it also harbors the machinery for the efficient packaging and infectious exposition of the genomic material. The beauty and elegance of the capsid structure and the intriguing processes of DNA packaging and unpacking provide inspiration for the design of artificial nanocapsules. In the present thesis, I summarize our efforts towards the understanding of the structure, nanomechanics and force-induced transitions of the T7 bacteriophage.

## 1.1 Icosahedral Capsid Architecture

In recent years, it has become increasingly recognized that the geometry of viral capsids plays an important role in their structural and mechanical stability. Virus capsids are broadly classified according to their shell structure. The majority of virus capsids have icosahedral structure[1,2]. The basic icosahedron has 30 edges, 20 triangular faces and 12 vertices. Thus, the underlying icosahedral lattice divides the capsid surface into 20 equal triangular parts. The icosahedron is a remarkably symmetrical object: it has $15 \times 2$-fold symmetry axes at the edges (180˚ rotation), $10 \times 3$-fold at the faces (120˚ rotation) and $6 \times 5$-fold at the vertices (72˚ rotation) (**Fig. 1.**). The triangular components bind to each other equivalently, thereby making the icosahedron a minimal-energy structure.
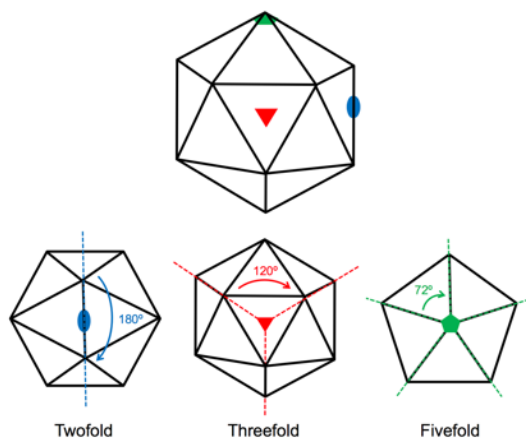


**Fig. 1.** Rotational symmetry axes of the icosahedron. The icosahedron viewed along the two-, three- and fivefold symmetry axes (left to right). The twofold axis passes through the middle of each edge, the threefold axis through the center of each icosahedral face and the fivefold axis through the vertices. Around the two-, three- and fivefold symmetry axis, 180˚, 120˚ and 72˚ rotation brings the object to self-coincidence, respectively.

Each triangular face contains one protein subunit in its corners, but the number of protein subunits between them increases with the capsid size. The maximum number of components that can be joined in an equivalent manner is 60, therefore one of them gives the structural unit of a virus shell. The simplest virus has capsids constructed of just 60 proteins but most have many more. Upon increasing the number of protein subunits, the binding between them cannot remain identical. Thus, they form pentamers and hexamers by joining 5- or 6-protein subunits, respectively.

In 1962 Caspar and Klug proposed the concept of quasi-equivalence to account for the arrangement of proteins on the icosahedral capsid surface[3,4]. The concept is based on the assumption that identical capsid protein subunits interact with each other, create nearly identical (quasi-equivalent) bonds to form icosahedral capsids. The triangulation number is a formal descriptor for complex icosahedral capsids which unambiguously describes the geometrical arrangement of protein subunits. The $T$-number can be calculated on a triangular lattice according to the formula

$$T = h^2 + hk + k^2, \tag{1.1}$$

where $h$ and $k$ are the lattice coordinates spanned by two unit-length vectors at $60°$ angle. The $h$ and $k$ numbers are the integer steps, made along the vectors separated by $60°$ on the triangular mesh, required to reach from a pentamer to an adjacent one (**Fig. 2.**).
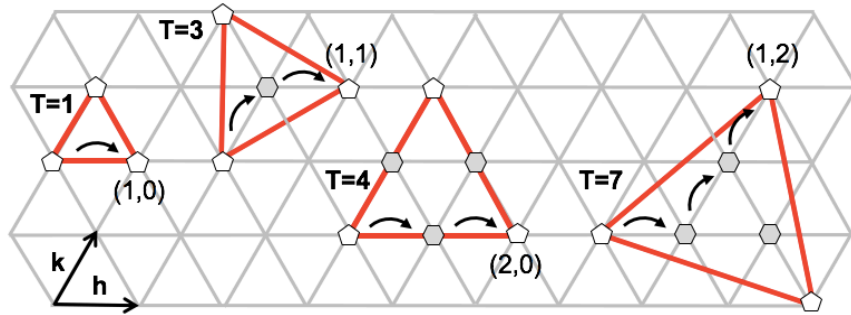


**Fig. 2.** Calculation of the triangulation number on a triangular lattice. The $h$ and $k$ axes are crossing at $60°$ angle and form equilateral triangles. The two unit vectors $h$ and $k$ of the hexagonal net define the coordinates. Hexamers and pentamers are located at the lattice intersection joints. The triangular facet of an icosahedron is indicated with red triangles.

The $T$-number indicates the number of unit triangles contained in an icosahedral face. In general, each unit triangle is formed of three protein subunits, but in some capsids the

position of the triangles does not coincide with the underlying protein subunits. In spite of this, the icosahedral shell has $60 \times T$ protein subunits in total and $60 \times \frac{T}{2}$ subunits per icosahedral face. As a pentamer is built up of 5 and a hexamer from 6 protein subunits, a capsomer shell contains at least 12 pentamers and $10 \times (T-1)$ hexamers.

The schematic capsid diagrams often show only the pentamers and hexamers, the building proteins of which may not coincide with the triangular lattice. In any case, the triangulation number can alternately be determined from the number of protein subunits of a single structural unit out of the 60 (**Fig. 3.**).
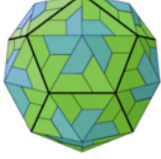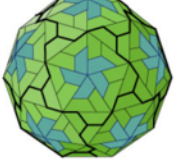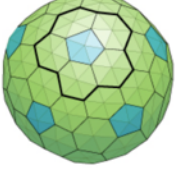


**Fig. 3.** Capsid structure according their triangulation number. (Source: ViralZone www.expasy.org/viralzone, SIB Swiss Institute of Bioinformatics)[5]

## 1.2   Bacteriophage T7 Structure

Our research group has had a long-time interest in the structure and stability of bacteriophage T7[6–10]. Bacteriophage T7 belongs to the *Podoviridae* family and infects most strains of *Escherichia coli (E. coli)*. The T7 bacteriophage is composed of a head with a

non-enveloped icosahedral capsid shell of $T = 7$ symmetry and a short non-contractile tail[11–14] (**Fig. 4.**).
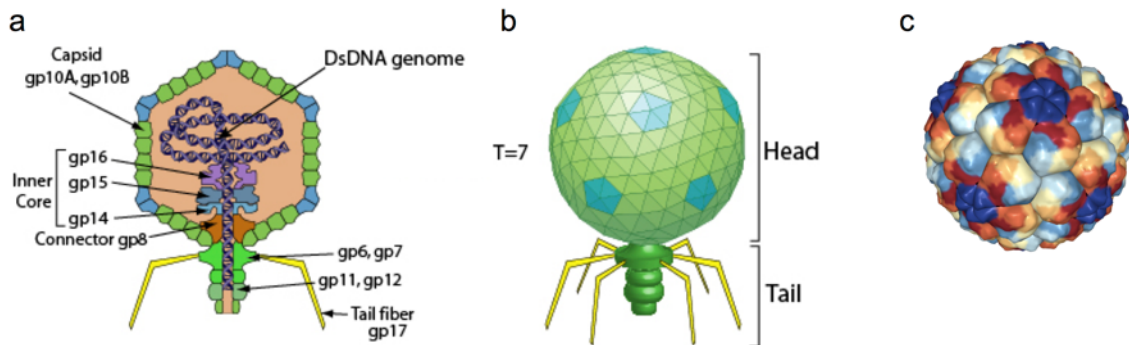


**Fig. 4.** Bacteriophage T7 structure. **(a)** Cross-sectional diagram and **(b)** schematic structural model of non-envelopped T7 bacteriophage. (Source: www.expasy.org/viralzone, SIB Swiss Institute of Bioinformatics)[5] **(c)** Atomic surface models of the T7 capsid structure derived from cryo-EM reconstructions. (Source: rcsb.org[15,16])

The head comprises an inner core and a shell. The inner core consists of gp14, gp15, gp16 and gp8 proteins, and the shell is an assembly of 415 pieces of gp10A structural proteins (note that *"gp"* stands for *"gene product"*). These structural proteins arrange into two types of capsomer subunits: 5-gp10A pentamers and 6-gp10A hexamers. The pentamers are located at 11 of the 12 icosahedral vertices, and the last vertex is occupied by the dodecameric connector protein gp8. The hexamers fill out the 60 topological locations around the pentamers. The mature capsid is filled with the 40 kbp-long genomic dsDNA.

## 1.3 Bacteriophage T7 Maturation

Virus maturation is a highly complex process which corresponds to a transition from a non-infectious immature particle to an infectious mature virion. In the first step, the assembly of the viral structural elements leads to the formation of immature DNA-free virus particles which are unable to initiate infection. The final stage of the assembly pathway of most viruses is followed by a set of structural transitions and biochemical modifications that transform the assembled particles into a mature infectious agent.

The maturation of dsDNA bacteriophages includes two major steps which share a surprising degree of similarity[12,17,18]. First, an icosahedral procapsid assembles from a limited set of structural proteins, followed by an ATP-driven DNA packaging and a drastic rearrangement of procapsid proteins that mature into an infectious phage.

The T7 procapsid assembles from certain number of main shell protein monomers (gp10), scaffolding proteins (gp9) and a dodecameric connector or portal (gp8) which attaches to a core complex (gp14, gp15 and gp16). These proteins must interact in a well-defined way to form a fully functional prohead with proper shape and size. The basic structure of these proteins is highly similar across different bacteriophages but the main protein fold may contain extra domains, which leads to a unique assembly mechanism.

The DNA packaging of T7 phage starts at procapsid state. The DNA packaging machinery is located at the same vertex as the portal and core complex, and is formed by ATPases (gp18 and gp19) which help the DNA pass through this entry tunnel. In this phase of the maturation, the scaffolding proteins also disappear and the drastic transformation of the shell begins.

By comparing the procapsid and the mature capsid the maturation process involves the increase of the shell diameter from 51 to 60 nm and the decrease in its thickness from 4.5 to 2.3 nm due to the rearrangement of the gp10 domains. The tertiary topology of gp10 monomer is divided into four regions: N-arm, E-loop, A-domain and P-domain. Maturation is the result of a series of changes between these structural elements (**Fig. 5**.[17,18]).
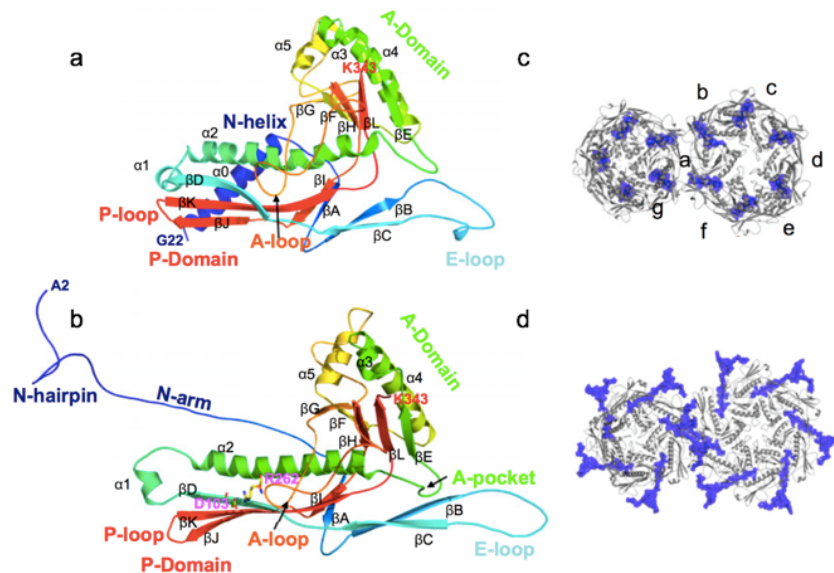


**Fig. 5.** Atomic models of major capsid protein gp10A. (**a**) gp10A subunit in procapsid (capsid I) and (**b**) in intermediate capsid (capsid II). The models are rainbow-colored from N (blue) to C (red) terminus. Arrangement of subunits in a pentamer (left) and a hexamer (right) of the (**c**) procapsid shell and (**d**) intermediate capsid shell. Subunits in (**c**) are indicated with lower case letters (a-g). The N-helix and N-arm regions are colored blue. All images are viewed from the capsid outer surface. Source:[18]

The A-domain bends in respect to the P-domain: its N-terminal region moves outwards, and the E-loop bends to further cover the monomer. The monomers perform translation, in-plane rotation and tilting which results in an expanded thinner shell with increased radius and capsomers with better symmetry. These changes reinforce the bonding lattice between the neighboring subunits, which is crucial to the formation of an infectious mature virion. The T7 has a different stabilization strategy than other bacteriophages. In general, bacteriophages have covalent cross-linkages (HK97) or bridging auxiliary proteins on the capsid surface (T4, λ) for the stabilization of the capsid shell. However, T7 phages use an intrasubunit salt bridge as an intracapsomeric topological linkage through the E-loop of neighboring subunits, and an intercapsomer joint-like interaction between a maturation-generated protein hairpin and a maturation-generated protein pocket[18]. For further stabilization of the capsid shell, mature bacteriophages also incorporate accessory proteins that can reinforce the contact between capsomers. T7 phage is distinct in this respect too, because it has no accessory proteins. The common step across phages, following the DNA packaging and capsid stabilization, is the tail attachment, which completes the maturation process.

## 1.4 Morphological and Mechanical Characterization of Single Virions by AFM

### 1.4.1 AFM Operating Principles

Atomic force microscopy (AFM) is a material characterization technique which allows to measure the topology and local material properties of surfaces and surface adsorbed samples with sizes that range from that of molecules to cells. In recent years, AFM has become an important tool in the investigation of viral structure and mechanics. Because of the central importance of AFM in my experimental approach, the method is detailed in the following. The operating principle of the AFM was first described by Binnig et al[19,20]. AFM operates with a sharp tip which is mounted at the end of a cantilever spring and is brought in close proximity with the surface area to be scanned (**Fig. 6.**). During scanning the interaction between the sample and the tip causes the cantilever to bend. This bending is detected by a laser beam which is focused on the back part of the cantilever and reflected to a quadrant photodiode.
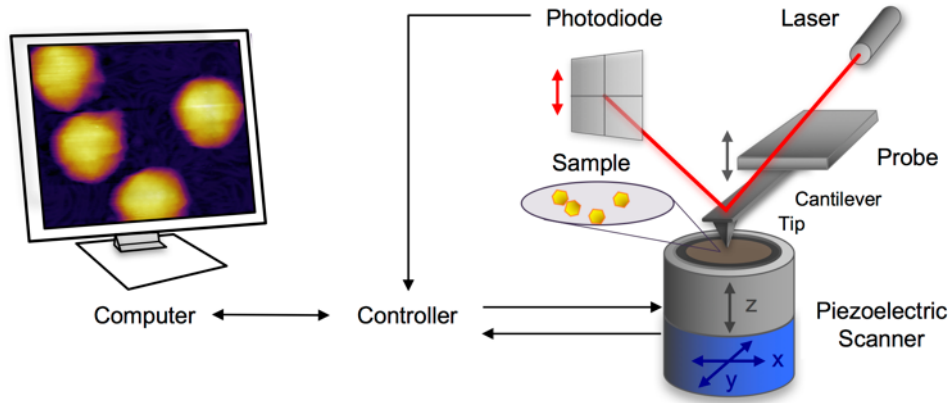
**Fig. 6.** Schematic diagram of a typical AFM measurement setup.

The nanometer-scale movement of the sample is provided by polycrystalline piezoelectric ceramics (piezo). These materials undergo a reversible deformation when an external bias voltage is applied across their two opposite faces. In order to construct real topological images of the samples, the AFM is equipped with two individual piezos. One generates the samples movement in the x-y direction, and the other one generates the z-direction displacement. The location of the z - piezos is dependent on the actual AFM design and may be attached either to the cantilever or the sample holder stage.

AFMs are generally designed with a distance between the cantilever and the photodiode detector that is orders of magnitudes larger than the length of the cantilever. This acts as an optical lever, which greatly magnifies motions of the tip, increasing the sensitivity and consequently the z-axis resolution.

The mechanical properties of the cantilever also determine the limit of the image resolution. Biological samples are soft, therefore cantilevers with low stiffness are preferable for imaging purposes as they exert lower forces on the sample. Typical commercially available cantilevers are made of silicon nitride and have a sharp tip at the end. The cantilever is either rectangular or V-shaped with a length of 100 - 200 μm, curvature radius of 8 - 20 nm and stiffness of 0.01 to 0.5 N/m. The typical cantilever resonance frequency ($f$) is between 15 and 500 kHz and depends on the stiffness ($k$) and mass ($m$) according to

$$f = \frac{1}{2\pi}\sqrt{\frac{k}{m}} \tag{1.2}$$

In liquids the cantilever resonance frequency becomes reduced. In order to nevertheless obtain high resonance frequencies and low stiffness (which are important for non-destructive imaging), strategies for decreasing the cantilever mass (hence, size) are being utilized. As a result, very small cantilevers are increasingly used for fast, high-resolution AFM imaging.

### 1.4.2   AFM Techniques

#### 1.4.2.1   AFM Imaging

The most widely used application of AFM is the imaging of surface-adsorbed samples where the x-y piezo provides the movement along the horizontal plane for scanning a selected area.

In order to achieve high-resolution images, the tip-sample force (or the oscillation amplitude described below in the *"AFM operating modes"* section) has to be maintained at a predefined constant low value (set point) independently of the topological variations of the surface. Therefore, when the sample height significantly changes during the lateral movement of the tip, its vertical position needs to be adjusted accordingly using the z-piezo. This is generally achieved with a tightly-controlled feedback loop which monitors the tip-sample interaction and lowers or elevates the tip to maintain the predefined set-point value. Such feedback system allows to follow the topography of the sample accurately and thereby increase the resolution of the imaging.

#### 1.4.2.2   Force Spectroscopy

Another major application of AFM is force "spectroscopy" where the cantilever is used as a piconewton-sensitive force probe by moving the tip along the vertical z-axis without scanning in the x-y plane. Although there is no true matter-radiation interaction, the name force "spectroscopy" is widely used.   Force spectroscopy measurements can be further categorized as stretching or indentation experiments, depending on whether the force exerted on the tip is measured by pulling a tip-attached molecule or by pressing a surface-attached sample.

In stretching experiments, the tip approaches the surface until it reaches and attaches to a molecule. Then the tip retracts from the surface, thereby pulling the molecule while registering a force-distance curve. Such force-distance curves provide information about the

structural transitions of the molecule such as protein unfolding, molecular interactions or binding properties. For certain special experiments the tip may be further chemically functionalized or mounted with special ligands to bind selectively.

In indentation experiments, the tip approaches the surface and exerts a predefined force on the sample while registering a force-distance curve. The generated force-distance curves provide information about the elastic properties of the sample.

The value of force ($F$) at any location is generally calculated using Hook's law:

$$F = kd, \tag{1.3}$$

which requires precise knowledge of the stiffness of the cantilever ($k$) and its deflection ($d$). There are several different methods for precisely determining the cantilever stiffness (spring constant) which fall into three main classes. The first is called loading method[21] which is based on exerting force on object with known stiffness by the unknown cantilever with unknown stiffness. From the recorded force-distance curve the cantilever's stiffness is calculated.

The second is the geometry method[22,23], which calculates the stiffness by measuring the cantilever dimensions and resonance frequency. The third and increasingly used method is called thermal calibration or thermal tuning, which is based on the thermal spectrum analysis of the cantilever[24].

In an acoustically isolated system, in which the cantilever vibrates only due its thermal energy and the cantilever moves only in z-direction, the thermal energy is equal to the elastic potential energy of the cantilever. Thus, according to the equipartition theorem:

$$\frac{1}{2} k_B T = \frac{1}{2} k \langle d^2 \rangle, \tag{1.4}$$

where $k_B$ is Boltzmann's constant and $T$ is the temperature, $k$ is the stiffness of the cantilever and $d$ is its deflection. For thermal tuning the deflection is recorded for a time interval with the cantilever in thermal equilibrium and constrained on only one end, oscillating at a distance away from any surface. Then the recorded time series is Fourier transformed and analyzed in the frequency domain to find the resonance frequency (frequency of the fundamental peak) and the power associated with the resonance. To accurately calculate the stiffness of the cantilever the laser displacement on the detector also needs to be calibrated

against the position- detector sensitivity. For this, static load is exerted at the end of the cantilever constraining it at both ends rather than only one end when the thermal energy was measured. The advantages of the thermal method are that it is independent of the material and shape of the cantilever, and it can be carried out relatively easy and fast.

### 1.4.3 AFM Operating Modes

Modern AFM devices provide several operating modes for imaging. The imaging modes are accordingly divided into two major types depending on which tip–sample interaction is detected **(Fig. 7.)**. The first mode is called static or DC mode, in which the tip is brought into contact with the surface and the static deflection of the cantilever is recorded. The second mode is called resonant or AC mode, in which the tip is forced to oscillate using a piezoelectric element, and the changes in its oscillation amplitude due to the tip-sample interaction forces are recorded. By partitioning an idealized curve of force between the tip and sample, different areas can be highlighted where the typical imaging modes operate[25].
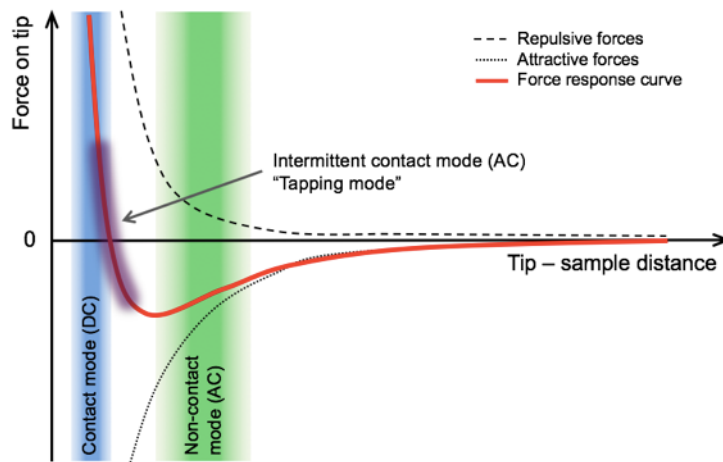


**Fig. 7.** Schematic plot of the forces between tip and sample, highlighting the typical zones for the different operating modes.

Static or DC mode can be further classified into contact, deflection and lateral force microscopy modes.

- Contact mode is the most commonly used DC mode, where the tip is in direct contact with the sample. During scanning the deflection is kept constant by a feedback loop. Because the tip is continuously in contact with the sample, shear forces are generated which may damage the sample. To preserve the integrity of soft biological samples

in this method as best as possible, soft cantilevers should be applied. Liquid environment can further reduce the stress on the sample by eliminating the capillary forces between the tip and the sample.

- Deflection or error mode is used for scanning rough or relatively rigid samples because the cantilever presses harder on asperities and less on depressions generating images with high-frequency information.

- Lateral force microscopy mode is applied when the samples have uniform, constant height but contains distinct areas with different frictional properties due to variation in chemical characteristics. In this case, the image is generated by detecting the torsion of the cantilever on the quadrant photodiode.

Resonant or AC modes can be further classified into non-contact, intermittent contact, phase imaging and force modulation mode.

- In non-contact mode, the oscillating tip is brought close to the sample surface without touching it, yet sensing the van der Waals attractive forces. The attractive forces induce a shift in the resonance frequency of the cantilever. During imaging the frequency shift is kept at a constant level trough continuously adjusting the surface-tip distance with a feedback loop by monitoring the amplitude at a particular frequency. This mode can be applied only to dry samples.

- Intermittent contact or tapping mode is similar to non-contact mode but approaching the sample and getting in contact with it, the repulsive force causes dampening in the oscillation amplitude (driving amplitude). In this method, the image is generated by keeping the decreased amplitude (setpoint amplitude) constant at the sample surface using a feedback loop. This mode of operation is widely used to study soft biological samples, because the vertical and lateral resolution are both high, and the interaction with the sample is weaker than with contact mode.

- Phase imaging can be performed during scanning with intermittent contact mode, by acquiring the phase difference between the driving signal and cantilever oscillation. The phase images provide information about local mechanical properties of the sample such as viscosity and adhesion.

- Force modulation mode works with low-frequency oscillation of the tip while keeping it permanently in contact with the surface. The varying stiffness of surface

features induces dampening of the cantilever oscillation, meanwhile the corresponding cantilever deflection is recorded. Thus, the recorded images give information about the local relative viscoelastic properties of the sample.

Force "spectroscopy" can be performed with either static or dynamic modes. The most preferred method is contact mode, where the deflection of the cantilever is registered as a function of its displacement as the tip approaches the surface, gets in contact with it and then retracts. In dynamic modes, information about the cantilever vibration is registered in addition to the static deflection and several parameters can be measured as a function of distance such as static deflection, amplitude, phase, higher harmonics or frequency. These data represent valuable information about the material properties such as short- and long-range forces, friction, plasticity and chemical composition.

### 1.4.4 Atomic Force Microscopy in Virology

One of the primary goals in virology is to reveal the mechanisms behind the intricate relationship between the structure and function of viruses. Atomic force microscopy is an effective technique that has been applied in this field fairly recently in order to understand the underlying details of such mechanisms. It allows not only to explore the structure of viruses but also to investigate their mechanical properties, which have been shown to be related to infectivity[26].

The structural exploration of viruses by AFM imaging started in the mid 1990s [27] and was followed by increasingly detailed description of numerous virus particles as the technique improved[28–47]. AFM imaging allows for the precise characterization of the capsid structure, such as the general dimensions, the arrangement of the capsomers and even the identification of underlying motifs. Two alternative techniques commonly used for examining virus structures are X-ray crystallography and electron microscopy (EM). These techniques are capable of giving information about the interior structure, but they also require specific sample preparation, such as aligning the virus particles into highly ordered formation for X-ray crystallography, or heavy metal staining, shadowing and vacuum drying for EM. By contrast, AFM imaging techniques require minimal preparation and can be applied under physiological conditions without any drying, fixing or staining. Recent advancements in cryo-EM, a special variant of EM, enabled detailed analysis of virus particles in close-to-native state. However, AFM imaging is still more universally suitable

15

for studying maturation[44], assembly[40,45,47], cell infection[29,35,41] and the effect of different environmental conditions[36]. Furthermore, force spectroscopy methods make AFM a uniquely attractive approach to investigate the mechanical properties of viral structures. Although, the first investigation of the elastic properties of viruses was performed in the late 1990s[48], their exploration by indentation experiments became widely employed only in the mid-2000s[26,49–79]. The AFM indentation experiments with varied parameters, such as applied force, loading rate or the number of cycles, provided increasingly detailed information about the

- mechanical properties of local structural differences of the capsid[59,60]

- role of internal DNA and protein-DNA interactions[49,51,52,55,72,76]

- mechanisms of maturation, assembly and DNA delivery[44,50,54,65,74]

- effect of different environmental conditions (pH, salt, host molecules, chemical stress)[44,69,71,73].

Recent AFM studies focus on manipulating the mechanical behavior of virus capsids through protein engineering[26,56,57,61,62,78,79] in order to reveal the role of the different structural motifs that may contribute to the development of virus-based nanoparticles[80–85] with improved mechanical properties. Notably, although the T7 bacteriophage has been investigated by a variety of methods, its exploration with AFM has so far been limited[44].

## 1.5 Bacteriophage T7 – Melting Experiments

Our research group has in the past investigated the structure and stability of the T7 bacteriophage, primarily with absorption spectroscopic methods[6–10]. It has been found, in optical melting experiments, that the T7 phage passes through two major temperature-dependent transitions (**Fig. 8.**). In these experiments, optical density (OD) of the sample at 260 nm ($A_{260}$) is measured while heating the sample from room temperature to 95 ˚C. Because it is DNA that absorbs at this wavelength, one may obtain insights about the overall structural changes of T7 through the changes in DNA. The first transition, which occurs at around 50-55 ˚C, is thought to correspond to the loosening of capsid structure so that the strain in DNA, due to the tight packing in the capsid is decreased, hence the $A_{260}$ is likewise decreased. The second transition, which occurs at around 80-85 ˚C, is thought to be

associated with strand separation of the dsDNA. Finally, the third transition appears at around 90-95 ˚C, and is related to the disruption of the alpha-helical protein structure.
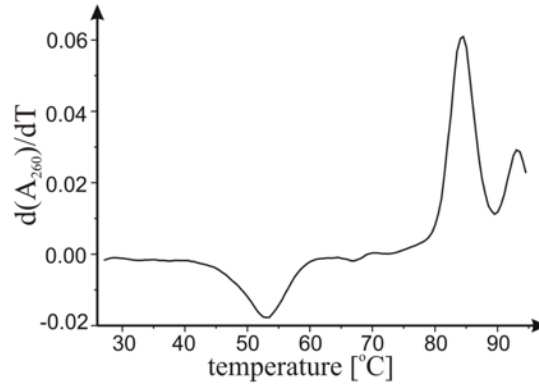


**Fig. 8.** Optical melting of the T7 bacteriophage. First derivative of the melting curve $A_{260}(T)$ is shown at 260 nm as a function of temperature for the range 25-95 ˚C.

The optical melting experiments clearly demonstrate that there is a change in the nucleoprotein structure upon increasing the temperature. However, due to the indirect nature of the method (i.e., changes in the optical properties of DNA, rather than the entire nucleocapsid, are recorded) and the fact that it is an ensemble technique (i.e., measurement values represent averages across the entire sample), the microscopic mechanisms of the induced changes remain hidden. We anticipated that by exploring the structure of individual T7 bacteriophage particles by using a high-resolution method such as the AFM, the mechanisms of the structural changes could be revealed.

## 2  OBJECTIVES OF THE THESIS

Although viruses are known to become inactivated by heat treatment, the mechanisms of the accompanying thermally-induced structural changes within the particles are not known. Furthermore, the dynamics of the capsid behavior and the mechanism of the DNA ejection process are still largely unresolved. Because AFM is an effective technique in our hands to explore the detailed structure of these nanometer-sized particles in various environmental conditions and also allows to investigate their mechanical properties, we endeavored to answer the following questions by using this technique:

- What kind of changes occur in the capsid structure due to heat-treatment?
- How do these structural changes influence the mechanical properties of the particles?
- How does the internal DNA contribute to the mechanical stability of the virus capsid?
- How do the mechanical properties of T7 phages relate to the topology and dynamics of capsomeric proteins and intercapsomeric interactions?
- What is the role of mechanical force in triggering DNA ejection of the T7 phage?

# 3   METHODS

## 3.1   Virus Preparation

T7 bacteriophage (ATCC 11303-B7) was grown in *Escherichia coli* (ATCC 11303) host cells and purified according to the established methods[86]. The phage suspension was concentrated on a CsCl gradient and dialyzed against buffer (20 mM Tris-HCl, 50 mM NaCl, pH 7.4)[7]. The T7 bacteriophage concentration was determined from optical density by using an extinction coefficient of $\varepsilon_{260} = 7.3 \cdot 10^3$ L/(mol·cm).

## 3.2   Surface Treatment and Sample Preparation for AFM

T7 bacteriophage stock solution was further diluted 100 times in PBS (137 mM NaCl, 2.7 mM KCl, 10 mM $Na_2HPO_4$, 1.8 mM $KH_2PO_4$, pH 7.4) prior to deposition. Due to the icosahedral shape of the virus particles the contact area between the capsids and the mica surface is small. Thus, we functionalized the mica in two steps to cross-link the capsid proteins to the surface[87]. This treatment improved the stability and reliability of the AFM imaging in liquids. The first part of the two-step surface modification was to place positively charged amino groups onto the mica by covalent attachment of silanizing agents or poly-L-lysine (**Fig. 9.**). These two different agents led to similar results, but required a slightly different treatment process. For silanization, a glass exsiccator was used in fume hood to ensure a separated and closed container for evaporation.

First, the exsiccator was purged with nitrogen gas for 2 minutes, then 150 μl of APTES ((3-Aminopropyl) triethoxysilane, (99%, Sigma-Aldrich, St. Louis, MO) and 50 μl of N,N-diisopropylethylamine (99%, distilled, Sigma-Aldrich) was placed into two small separate containers. Next, the exsiccator was purged again with nitrogen for an additional 2 min and freshly cleaved mica was placed near to the containers. Following another 2 min purging with nitrogen, the exsiccator was sealed off while leaving the mica exposed to APTES vapor overnight. The mica (AP-mica) was stored in sealed exssicator until the next treatment step. The alternative poly-L-lysine (PLL, Sigma-Aldrich, St. Louis, MO) treatment started with the deposition of the undiluted solution onto freshly-cleaved mica, and after 15 min incubation it continued with rinsing 3 to 5 times with 100 μl of milliQ water and finished with drying the surface by gentle stream of nitrogen or air from aerosol duster.
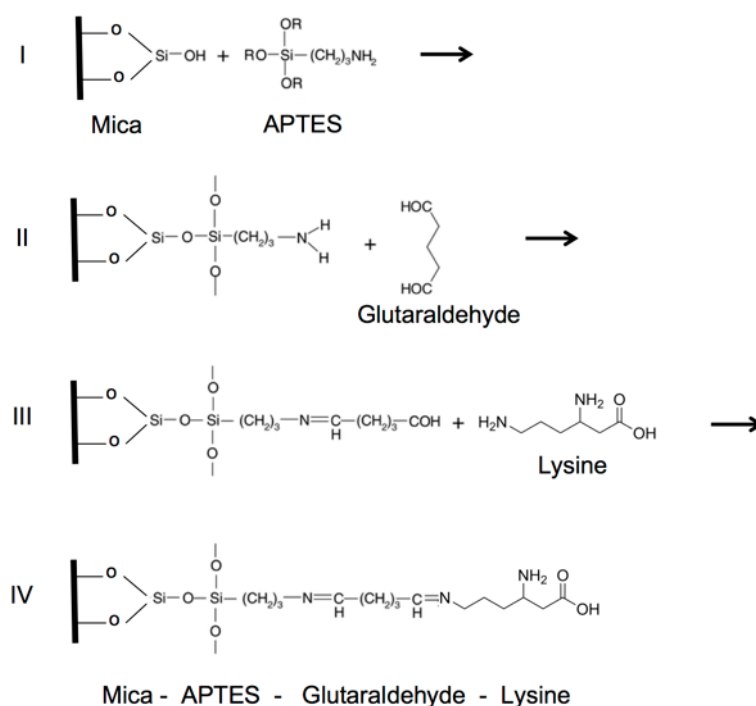
**Fig. 9.** Steps of glutaraldehyde cross-linking to the lysine residues of virus capsid. Mica reaction with APTES (I.), APTES amino group reaction with glutaraldehyde (II.), aldehyde group reaction with lysine (III.), crosslinked lysine residue (IV.).

The second part of the two-step surface modification process was the binding of zero-length cross-linker glutaraldehyde onto the modified AP-mica. This reagent forms stable binding with lysine residues of the sample. In this procedure 100 μl of 5% w/v glutaraldehyde (grade I, Sigma-Aldrich) solution was pipetted onto the previously modified mica immediately after the removal from the exsiccator. After 30 min incubation it was rinsed 3 to 5 times with 100 μl milliQ water and dried with a gentle stream of air from aerosol duster or nitrogen. **Fig. 9.** shows the steps of surface modification and the binding with the sample. The glutaraldehyde-treated mica (GD-mica) was always prepared freshly before the incubation of the virus solution.

## 3.3    AFM Imaging of Virus Particles

Non-contact mode AFM imaging and nanoindentation experiments were performed with an Asylum Research Cypher instrument (Asylum Research, Santa Barbara, CA). The diluted T7 bacteriophage sample was applied to functionalized GD-mica. Unbound viruses were removed by gentle washing with PBS after 30-60 min incubation. The surface-attached particles were scanned in PBS buffer using non-contact mode. In order to preserve the

integrity of the particles and keep them bound stable to the surface, a force well below 100 pN was used by setting the free amplitude and setpoint of the cantilever low.

For high-quality imaging, we used silicon cantilever (Olympus BL-AC40TS-C2) with an 8 nm radius tetrahedral tip (**Fig. 10.**). The $512 \times 512$-pixel images were collected at a typical scanning frequency of 0.6–1.5 Hz. For temperature-dependent measurements we used the BioHeater module of the AFM instrument to heat up the surface attached particles to either 65 or 80 ˚C for 15 min. The temperature was kept constant with a precision of 0.1 ˚C. The heat-treated samples were cooled back to room temperature prior to imaging and nanomanipulation.
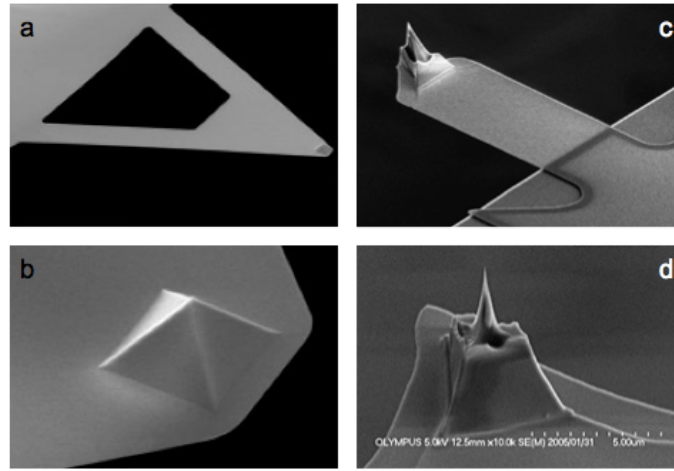


**Fig. 10.** SEM images of triangular (**a,b**) and conical (**c,d**) AFM cantilevers. For force measurement pyrex-nitride Nanoworld cantilever (PNP-TR) was used with pyramidal tip (**b**) with radius of <10 nm. For imaging silicon Olympus BL-AC40TS-C2 cantilever was used with an 8 nm radius tetrahedral tip (**d**). (Source: http://www.afmprobeshop.com)

## 3.4   Image Analysis

The images acquired by AFM scanning provide rich topological information of the surface-attached samples. Subsequent image analyses allow to measure the different features of the samples and to compensate for measurement artifacts. The generally conical or pyramidal shape of the tip causes lateral expansion of the features on the image. This tip-sample geometrical dilation is non-negligible when the dimension of the surface asperities or the sample size are comparable with the tip radius. **Fig. 11.** shows the geometric parameters associated with the dilation process. This effect is significant when scanning viruses because the tip radius (8 mm) and the particle diameter (50-60 nm) are of the similar order of

magnitude. The effect of such dilation can be corrected with post-processing. On the other hand, the height of the samples relative to the mica surface can be determined with subnanometer precision. Since the T7 bacteriophage is a spherical particle, its diameter can be precisely determined based on height measurements only. The height profile of an arbitrarily chosen region of the image can be evaluated using the AFM controller and analysis software (IgorPro v6.34A, Wavemetrics, Lake Oswego, OR). The height of the particles was always measured individually relative to the mica surface level directly surrounding it.
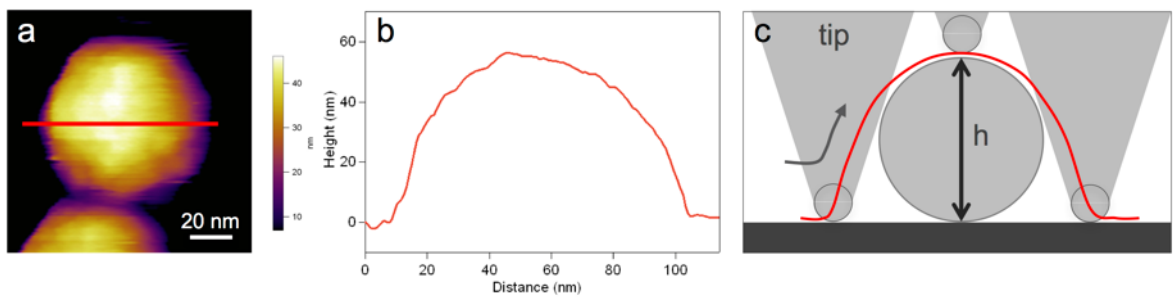


**Fig. 11.** Sample dilation due to tip convolution. Height-contrast AFM image of a virus particle attached to mica (**a**). Red line shows the chosen area on the image along which the height profile was plotted (**b**). Geometric parameters associated with the dilation process (**c**). The red line depicts the dilated profile/image section/line scanned by a triangular AFM tip.

### 3.5    Calculation of force exerted by the oscillating cantilever on the capsid

In order to calculate the average force on the capsid exerted by the oscillating cantilever, we carried out an empirical calibration procedure for each cantilever used. In this procedure the oscillating cantilever was pressed against a rigid control (mica) surface. Then the force was measured as a function of the detected cantilever oscillation amplitude. The stiffness-calibrated cantilever (Olympus BL-AC40TS-C2) was oscillated at its resonance frequency (20-27 kHz) by using photothermal excitation (BlueDriveTM) with a free amplitude of 100 mV, which corresponded to an amplitude of 2.5-3.5 nm depending on cantilever parameters. Stiffness calibration of the cantilever was carried out by using the thermal method[24]. The cantilever was moved with a constant rate (50 nm/s) towards the surface and both the average force and the oscillation amplitude (in terms of both position-sensor voltage and absolute distance) were measured. A calibration curve so obtained is shown in **Fig. 12.** By selecting an amplitude set- point for the feedback of the AFM imaging, we

adjusted the average force, exerted by the cantilever on the capsid, between approximately 10 pN and 40 pN.
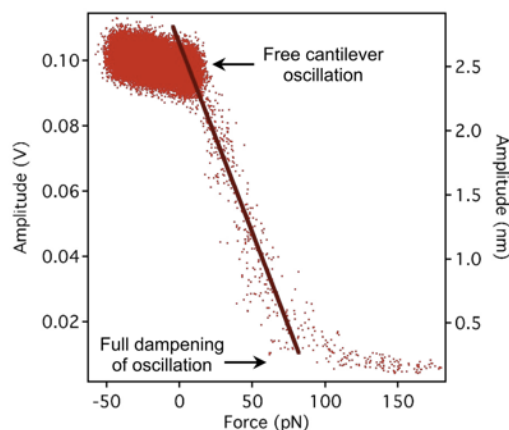


**Fig. 12.** Calibration curve of the average cantilever force as a function of oscillation amplitude expressed either as position-sensor voltage (left axis) or absolute distance (right axis).

### 3.6 Indentation Experiments on Virus Particles

Prior to starting the indentation experiment the virus particles were scanned to verify their intactness, locate single particles and position the tip above the center of the selected particle. First, the viruses were manipulated by pressing the cantilever tip against the apex of the particles until reaching a predefined maximal force, then pulling it back with a constant pre-adjusted rate. The typical velocity of the cantilever was 1 μm/s. The indentation experiments were also carried out in PBS buffer using a pyrex-nitride cantilever (Nanoworld PNP-TR, pyramidal tip, radius <10 nm, **Fig. 10.**). This tip was suitable to these experiments because it was both sharp and its nominal stiffness was stiff enough (0.3 N/m) to indent the relatively hard virus particles. As the output of the indentation experiment force-distance curves (FZC) were recorded. FZC involves the bending of two spring in series, that of the cantilever and of the virus particle. To remove the unwanted effect of cantilever bending in the FZC curve, a calibration curve was recorded on the solid mica surface. The force-deformation curve (FDC), which shows the force as a function of only the indentation of the particle, was obtained by subtracting this calibration curve from the original FZC. The stiffness was determined for each cantilever using the thermal method.

## 3.7 Indentation Experiment Analysis

Analysis of the FDC curves gained by indentation experiment provides information about the mechanical properties of the capsid [58]. **Fig. 13.** shows the experimental setup of an indentation, demonstrating the movement of the AFM probe and the corresponding curves.
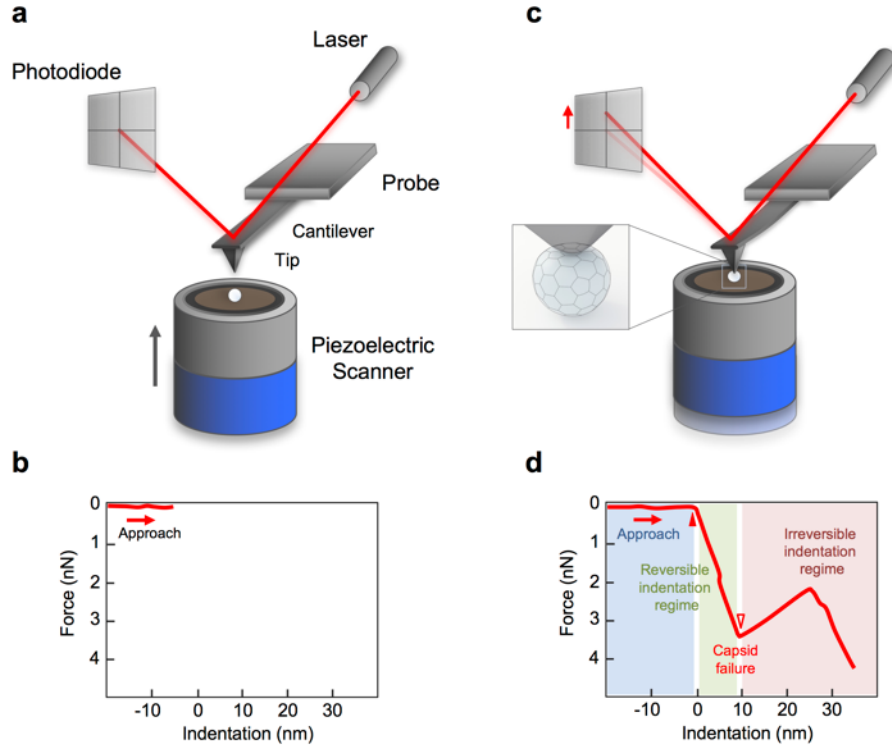


**Fig. 13.** Schematic diagram of AFM nanoindentation of a virus. (**a**) The piezo is extending but the AFM tip has not yet reached the virus surface and (**b**) therefore the exerted force is zero. (**c**) The AFM tip indents the virus particle while the cantilever bends; the exerted force on the tip is measured by the changes of laser signal detected on the quadrant photodiode. (**d**) The indentation force is plotted as the function of indentation depth.

**Fig. 13.d** shows a schematic FDC curve as a result. The curve has three main regions. When the tip is approaching the surface by extending the z-piezo, the force is zero because the tip is not in contact with the sample, hence the cantilever does not bend. From the point when the tip reached the capsid (**Fig. 13.d** filled/solid triangle), force begins to rise. Initially the force curve displays a linear regime with positive slope which corresponds to the deformation of the virus as a Hookean particle. The slope of this linear section yields the stiffness of the particle. When the capsid is unable to withstand further loading, the force abruptly drops, which corresponds to the capsid fracture (**Fig. 13.d** open triangle). The regime immediately following capsid breakage corresponds to the unloaded swinging of the

cantilever towards its equilibrium position. Accordingly, the slope of this region is equal to cantilever stiffness. Subsequently the force may begin to rise again. In this final region the mechanical properties of the broken capsid are manifested. In addition to the determination of the stiffness, the indentation depth (the distance between the contact point and the capsid failure, **Fig. 13.d** width of the green area) and the corresponding breaking force give further information about the capsid mechanical characteristics.

### 3.8    Analysis of steps in force spectra

In the force spectra we often observe stepwise transitions. These transitions cause discrete indentations of different magnitude. To obtain the distribution of the steps with minimal bias, we applied the following procedure of data analysis. First, the raw step-size data were sorted in increasing order. Second, a monotonously increasing sequential number *versus* distance curve was generated. Third, from this curve, after normalization by dividing each sequential number with the maximal sequential number, the cumulative distribution function of the dataset was computed (**Fig. 14.a**). Finally, the smoothed derivative of the cumulative distribution function was computed, which yielded the density function of the distribution. This distribution was fitted by multiple Gaussians without any preconception (**Fig. 14.b**). Following numerical integration of all the fitted Gaussians we obtained the calculated cumulative distribution function (**Fig. 14.a**). Subtracting the cumulative distribution function of the dataset from the calculated one, we computed the residue which slightly fluctuated around zero, proving the goodness of fit.
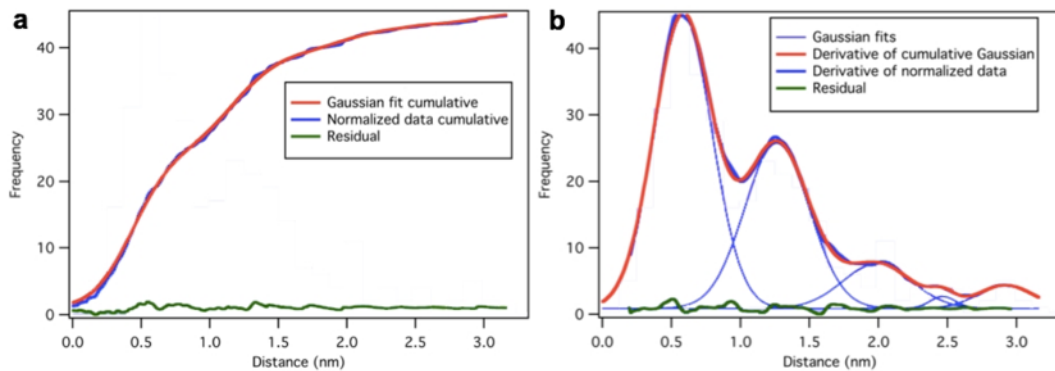


**Fig. 14.** Analysis of step data in the force spectra. (**a**) The integrated Gaussian-fit data (red) overlaid on the normalized cumulative step-size dataset (blue). Residual (green) curve shows the difference of the two curves. Histogram data is highlighted in the background for reference. (**b**) Gaussian fits (thin blue lines) and their sum (red) overlaid on the derivative of the normalized cumulative dataset (blue).

# 4 RESULTS

## 4.1 Temperature-Dependent Topography and Nanomechanics of Bacteriophage T7

### 4.1.1 Topographical Structure of Heat-Treated T7 Phages

To explore the heat-induced topographical changes in T7 bacteriophages, we exposed them to two-stage thermal treatment (65 ˚C, 80 ˚C) and studied the temperature-induced effects on the capsid using AFM. Previous UV absorption and CD spectroscopic melting experiments showed that the T7 bacteriophage releases most of its DNA in a transition occurring between 50 and 60 ˚C [6–9]. A second transition occurs at a temperature above 80 ˚C and it is related to DNA denaturation. Recent atomic-force and electron microscopy and calorimetric measurements have also revealed thermally induced DNA release in other viruses[88–94]. Since the absorption melting experiments gave us information about the virus particles only through the structural changes of their DNA, we decided to explore the thermally-induced changes in the capsid proteins using AFM. During the temperature-dependent experiments the sample was incubated for 15 minutes at either 65 or 80 ˚C, then cooled back to room temperature for AFM imaging (**Fig. 15.a**).

First, mature T7 phage particles containing 40 kbp-long genomic DNA cross-linked to GD-mica were imaged with AFM to obtain information about their morphological properties. Imaging was carried out in buffer using tapping-mode to allow accurate control of the maximal tip-sample force. Applying low force to the sample during scanning helps to keep the particles intact and attached to the surface. At room temperature, the virus particles exhibited an intact, sphere-like structure in the AFM images (**Fig. 15.a**). Furthermore, using a sharp tip allowed us to resolve the cogwheel shape and the central pore of the capsomers and, thereby, to identify the adsorbing symmetry of the capsids (**Fig. 15.d**)[44]. Around some virus particles, DNA clusters were showing on the surface due to occasional mechanically-induced DNA ejection. The conical tail complexes also became visible at different locations on most phage particles, depending on their binding orientation (**Fig. 15.b**). In the background, there were a few globular particles apparent, which may correspond to the core T7 phage proteins that got ejected simultaneously with DNA.
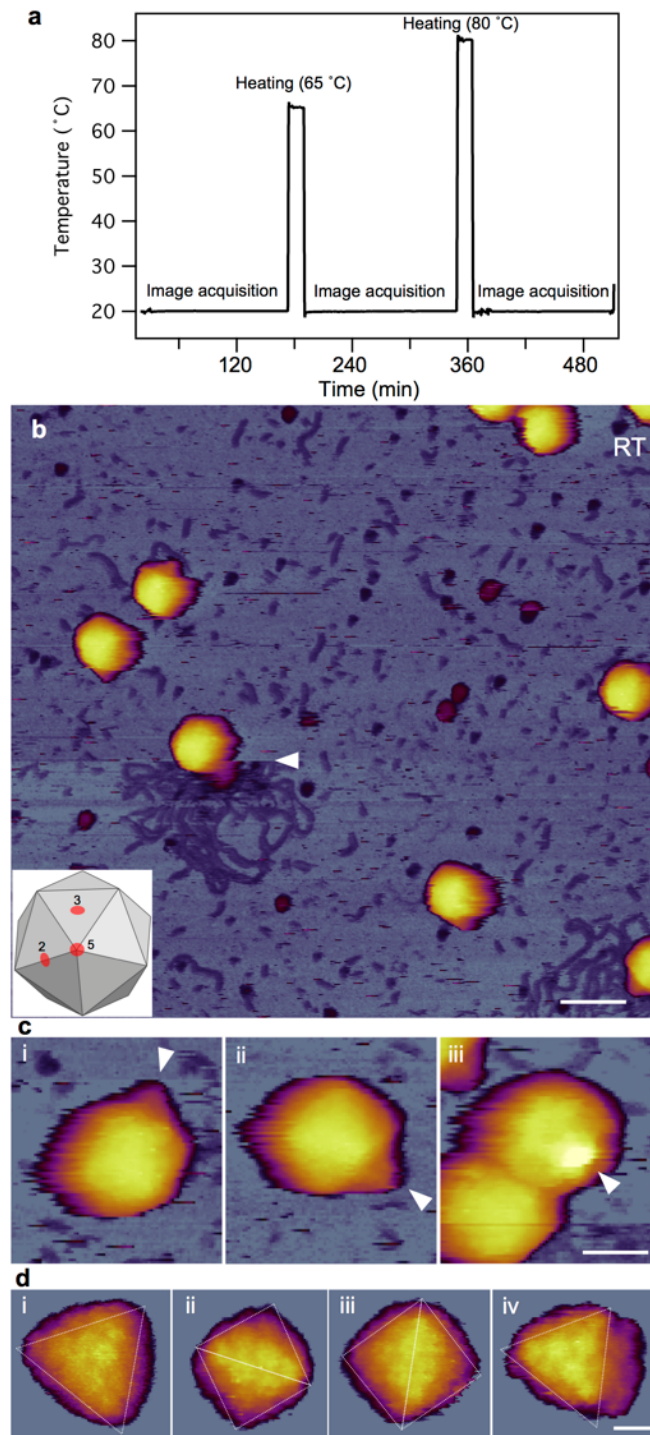
**Fig. 15.** AFM imaging of surface-immobilized untreated T7 bacteriophages at room temperature (20 ˚C). (**a**) Thermal profile of sample treatment protocol. (**b**) Overview of a 1 µm x 1 µm sample area. Slow AFM raster scan direction is from top to bottom of the image. White arrowhead points at the nearly instantaneous event of mechanically induced DNA ejection. Scale bar 100 nm. (**c**) AFM images of T7 phage particles displaying their conical tail in different orientations. White arrowheads point at the tail apices. Scale bar 30 nm. (**d**) High-resolution AFM images of the T7 phage surfaces with resolvable capsomers. Views along the two-fold (ii, iii) and three-fold symmetry axes (i, iv) are shown. Scale bar 10 nm.

Following the topographical exploration of the capsid structure at room temperature, we heated the same sample to 65 ˚C for 15 min then cooled it back to 20 ˚C for image acquisition (**Fig. 15.a**).  Upon 65 ˚C treatment, the topography of the sample has changed significantly (**Fig. 16**) The most apparent change is that the substrate surface became covered with a meshwork of DNA. The cross-sectional height profile of the background showed that the height of an individual strand is around 2 nm (**Fig. 16.a inset**), which closely matches the diameter of DNA. This shows that the DNA was indeed released from the capsid due to the heat treatment, as suggested earlier[8]. The second remarkable change in the images is that the conical tail complex of most capsids disappeared. Even where the tail was visible, its shape was stubby and lost its conical nature (**Fig. 16.b**). Thus, we speculate that the DNA has been released from the particles because of a separation of the tail complex from the capsid. Considering that the gp8 protein plays an important role in connecting the tail complex to the capsid, we hypothesize that it might be a thermally sensitive component of T7 phage. We also found large (>10 nm) globular particles in the background which may correspond to the residues of the tail complexes that broke off. The third change compared to the non-treated particles, is that the capsid surface became more faceted as the icosahedral edges and faces got more pronounced, which could be explained by a slight shrinkage of the capsid due to the DNA release (**Fig. 16.d-e**). Despite all these changes, the cogwheel shape of the individual capsomers remained intact (**Fig. 16.c**). In a few capsids, we noticed gaps in the position of the pentamers, which we identify as the exit holes through which DNA escaped (**Fig. 16.d**)
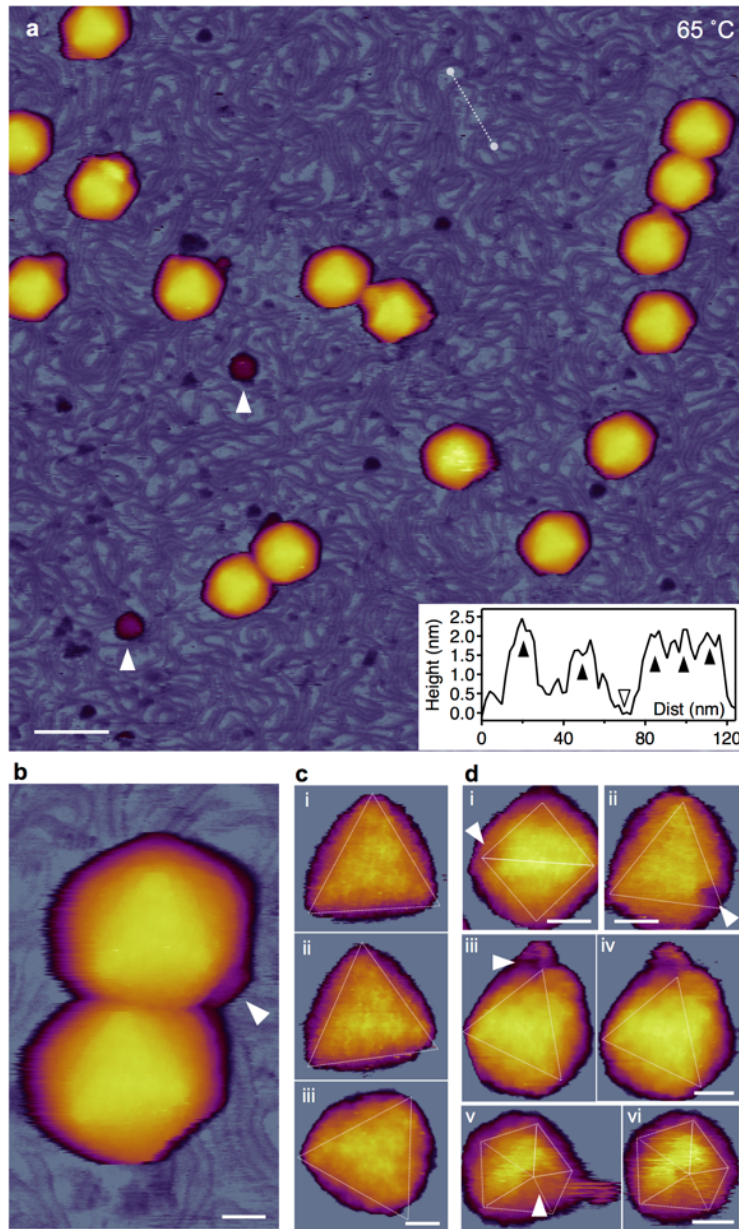
**Fig. 16.** AFM imaging of T7 phages treated at 65 ˚C. (**a**) Overview of a 1 μm x 1 μm sample area. White arrowheads point at large (>10 nm) globular particles. Scale bar 100 nm. **Inset**, topographical height map along an arbitrarily chosen line in the background (white dashed line). Black arrowheads point at DNA cross-sections, whereas the empty arrowhead at the substrate (mica) surface. (**b**) AFM image of two T7 particles. White arrowhead points at the short, stubby tail complex visible on one of the particles whereas there is no visible tail on the other one. Scale bar 20 nm. (**c**) T7 phage particles with resolvable capsomers on their surfaces. Views are along the three-fold symmetry axes. Because of contrast enhancement, only the top facets are visible and the rest of the capsid is hidden. Scale bar 10 nm. (**d**) T7 particles with resolvable DNA exit holes (white arrowheads). The exit hole appears as a gap at the location of a missing pentagonal capsomer at one of the icosahedron vertices. Images viewed along the two-fold (i), three-fold (ii, iii, iv) and five-fold symmetry axes (v, vi) are shown. Images (iii) and (v) are reconstructed from the rightward fast AFM scanlines, whereas images (iv) and (vi) are from leftward (reverse) scan lines from the same sample area. Scale bars, 20 nm.

Following the topographical exploration of the capsid structure treated at 65 ˚C, we exposed the samples to 80 ˚C temperature and imaged them after cooling back to room temperature (**Fig. 15.a**). In this case, the background was even more densely populated with DNA strands (**Fig. 17.a**). In addition, we observed a large number of globular particles, as well as large aggregates scattered in the background (**Fig. 17.b**). Given that the size of these aggregates far exceeds that of the tail complex and they consist of globular particles, we hypothesize that they originate from the capsid wall. Furthermore, in high-resolution AFM images the capsomers appear swollen with less distinct cogwheel structure (**Fig. 17.c**).
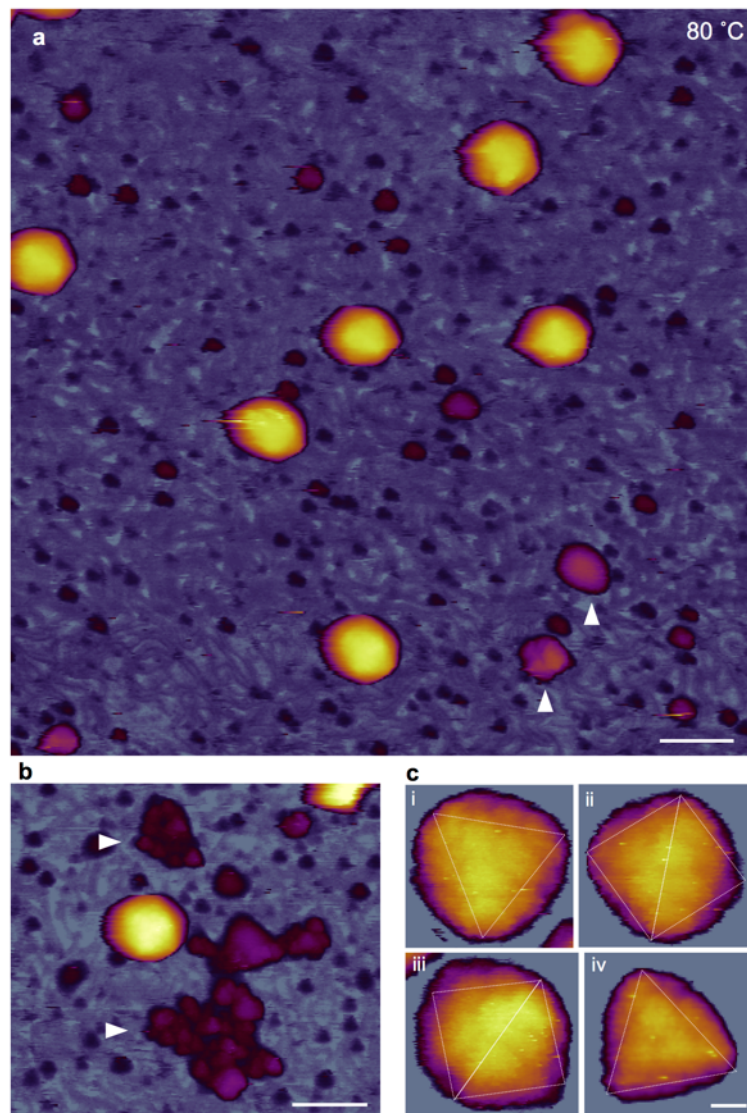


**Fig. 17.** AFM imaging of T7 phages treated at 80 ˚C. (**a**) Overview of a 1 μm x 1 μm sample area. Scale bar 100 nm. (**b**) White arrowheads point at large (>10 nm) globular particles. (**c**) High-resolution AFM images of 80 ˚C -treated particles with resolvable capsomers on their surface. Views along the three-fold (i, iv) and two-fold symmetry axes (ii, iii). Scale bar 10 nm.

## 4.1.2 Nanomechanics of Heat-Treated T7 Phages

Following the topographical exploration of the heat-treated particles, we manipulated them with AFM to reveal the thermally-induced changes in their nanomechanical properties. We performed indentation experiments by pressing the surface-immobilized particles with a sharp tip at their center along the z-axis (see details in **Materials and methods**). The maximal force was pre-adjusted to 10 nN, sufficiently high to achieve the total rupture of the particles in order to register their overall mechanical response. The results obtained on phages at room temperature (RT) are shown below (**Fig. 18.**).
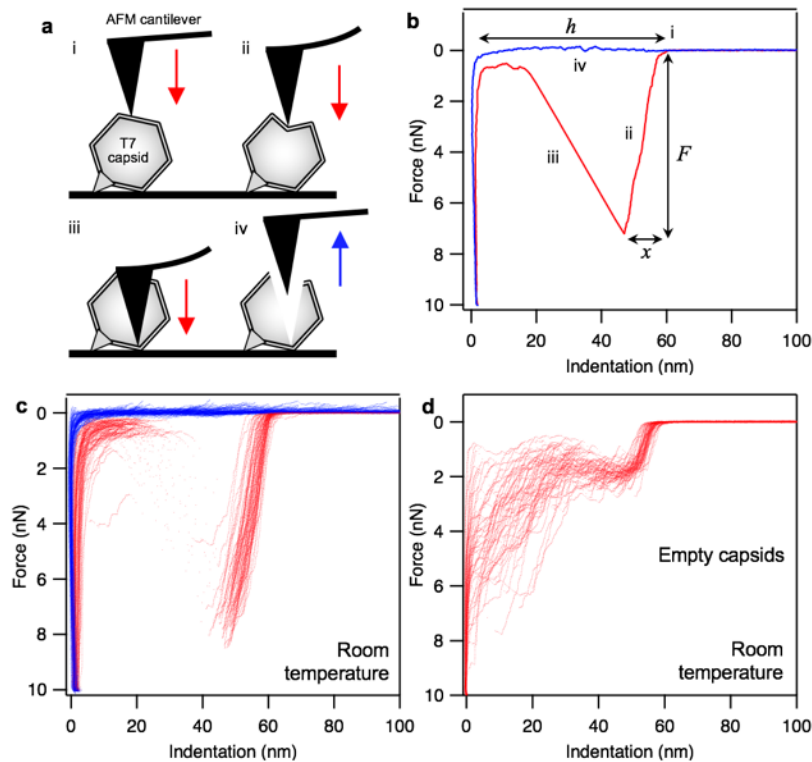


**Fig. 18.** Nanomechanics of T7 phages. (**a**) Schematic diagrams of mechanical manipulation (**b**) Representative force versus indentation curve obtained at room temperature. Red and blue traces are indentation and retraction half cycles, respectively. Notable stages of the nanomechanics experiments are marked with small Roman numerals (i-iv). Variables extracted from the data (breaking force F, maximal indentation distance x, capsid height h) are shown with italic letters. (**c**) Overlay of 80 similar force versus indentation curves collected in independent experiments on different phage particles at room temperature. (**d**) Overlay of 55 similar force versus indentation curves (indentation half cycle only) collected at room temperature in independent experiments that are similar to each other but are distinctively different from the dataset in (**c**).

The initial contact of the AFM tip with the capsid corresponds to an "elbow" in the FDC curves at around 60 nm (**Fig. 18 i**), followed by a linear section associated with the reversible regime of the capsid deformation (**Fig. 18 ii**). Increasing the load to around 8nN, the force

abruptly dropped, which marks the failure and collapse of the capsid (**Fig. 18 iii**). Further pressing the tip, the force fluctuated below 2 nN, then it began to rise sharply as it reached the substrate surface. The retraction force trace was essentially featureless (**Fig. 18 iv**), indicating that the conformational change of the capsid was irreversible. Although for the majority of the capsids similar force traces were recorded (**Fig. 18.c**), a fraction of them were significantly different and had reproducible appearance (**Fig. 18.d**). In the latter traces the initial linear regime ended at around 2 nN, we refer to these as putative empty capsids.

The force traces of capsids treated at 65 ˚C (**Fig. 19.a-b**) were similar to those of empty capsids, as the capsid breakage occurred at around 2 nN and then the force fluctuated before abruptly increasing as it reached the substrate surface. For the force traces of capsids treated at 80 ˚C (**Fig. 19.c-d**) the overall appearance was similar to that seen for the 65 ˚C -samples, but the capsid breakage and the following force fluctuation occurred at greater force levels.
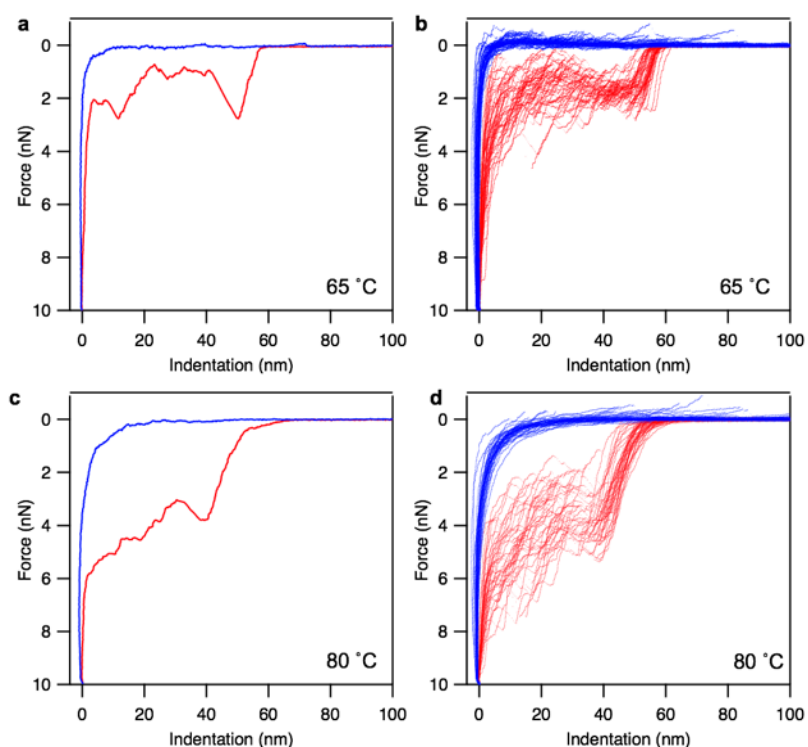


**Fig. 19.** Nanomechanics of heat-treated T7 phages. (**a**) Representative force *versus* indentation curve measured on a T7 phage particle that has been exposed to 65 ˚C temperature for 15 minutes. Red and blue indicate indentation and retraction half-cycles, respectively, throughout all figures. (**b**) Overlay of 45 similar force *versus* indentation curves collected in independent experiments on different phage particles heat-treated at 65 ˚C. (**c**) Representative force *versus* indentation curve measured on a T7 phage particle that has been exposed to 80 ˚C temperature for 15 minutes. (**d**) Overlay of 41 similar force *versus* indentation curves collected in independent experiments on different phage particles heat-treated at 80 ˚C.

## 4.2 Force-Induced Structural Changes of the Bacteriophage T7

### 4.2.1 Discrete Stepwise Transitions

To study the mechanical stability of the phage particles, we performed fatigue experiments by repeatedly applying load with a maximal 1.5 nN force, lower than the average breaking force (7 nN). This loading force created an approximately 10 nm maximal indentation and is low enough to prevent capsid failure during the first load, but sufficiently high to induce it after multiple cycles.

The repeatability of indentation cycles before the capsid failure corresponds to the fatigue of the capsid.

In an approximately one-fifth of the indented phage particles the force traces contained multiple discrete, step-like transitions (**Fig. 20.**). Although previous nanoindentation experiments of viruses made note of transient breakage points and transitions along the reversible indentation regime, they have not been analyzed systematically and in details.

Transitions typically appeared as a sequence of sawtooth-like features, peaks followed by a sudden transient drop in force. After a sawtooth-like feature the force continued to rise linearly again until the next peak or the breaking point. The slope of the linear sections between the peaks was unaltered indicating that in spite of the transitions, the global elastic properties of the capsid remained.

The number of the subsequent curves often reached up to one hundred before it resulted in capsid failure and the curves systematically contained these saw-tooth like steps (**Fig. 20.b**).

The repeatability of the indentation force traces and the recurrence of the transitions indicate that the capsid recovered from the force-induced structural changes on the time-scale of the experiment (10 ms).

The distribution analysis of the transition step-sizes (see in **Materials and methods**) showed peaks at integer multiples of approximately 0.6 nm (0.58 nm ± 0.21, S.D). This suggests that a single transition corresponds to a ~0.6 nm shift of the capsid structure, which might correspond to a slight, discrete structural change closely related to the capsomers.
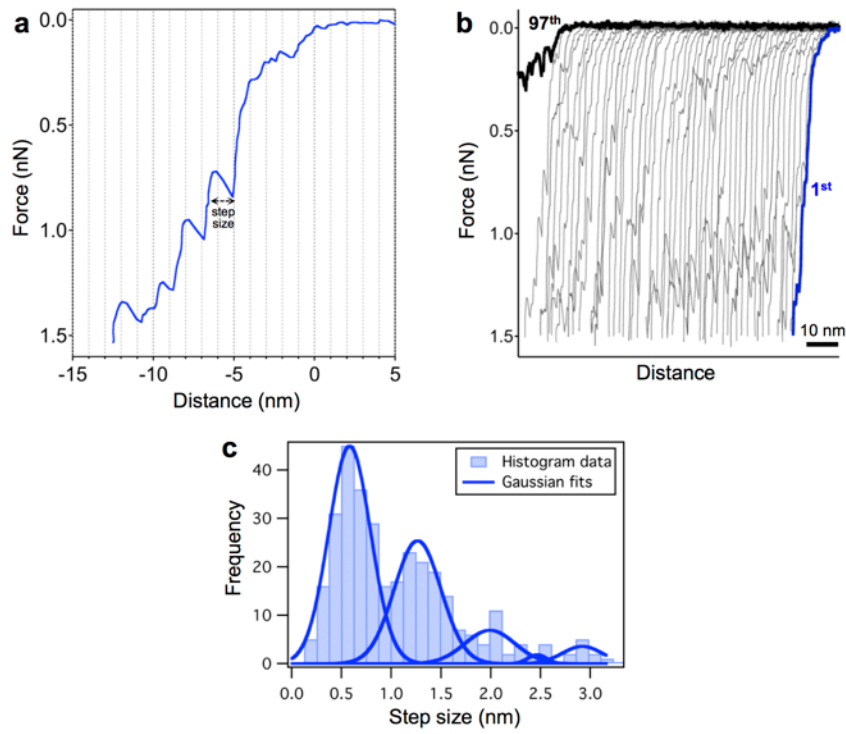
**Fig. 20.** Stepwise transitions and mechanical fatigue of T7 bacteriophage capsid. (**a**) Representative force versus distance curve obtained by indenting the capsid. Step size was measured as the distance change at the force of the sawtooth peak. (**b**) 97 consecutive FDCs collected on the same capsid at room temperature. The consecutive curves were shifted along the distance axis by 2 nm for better display. (**c**) Distribution of the transition step size with the fitted Gaussian curves. The peaks are centered at 0.58 (±0.21), 1.26 (±0.24), 1.99 (±0.25), 2.47 (±0.09) and 2.92 (±0.19) nm.

### 4.2.2   Rate Dependence of the Stepwise Transition

To gain further insight into this structural consolidation process we examined the retraction force traces corresponding to the previously analyzed indentation traces (**Fig. 21.a**). The trace and retrace curves showed similar discrete step-like transitions that aligned with some hysteresis, although the direction of their pathway was reversed. The time duration of the transition steps in the retraction traces was less than 10 ms, which indicates that the structural consolidation was rapid and proceeded against force.

To estimate the energetic topology of the mechanically-driven transitions, we performed dynamic force spectroscopy experiments using different loading rates in the range of 0.1 to 5 μm/s (**Fig. 21.b**). Towards the higher loading rates the hysteresis area increased (**Fig. 21.b**) due to the simultaneous increase of the indentation-step forces and the slight decrease of the retraction-step forces.

34
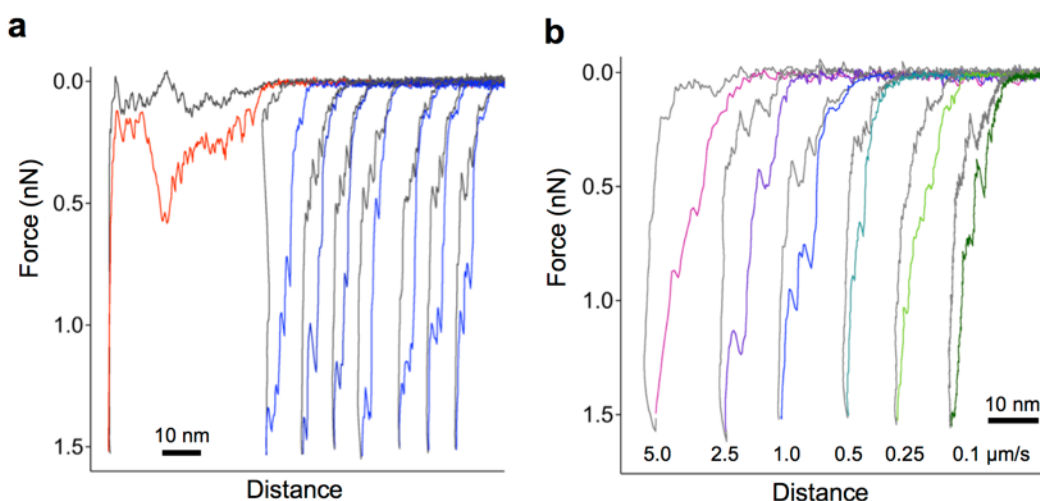
**Fig. 21.** Reversibility and rate-dependence of the stepwise transitions. (**a**) Representative indentation (blue) – retraction (gray) force *versus* distance curves obtained in consecutive trials on a T7 bacteriophage. The curves were shifted progressively along the distance axis for clarity. The red trace corresponds to the indentation force curve of capsid breakage. (**b**) Indentation – retraction force traces collected using different cantilever velocities (values indicated in the figure in μm s$^{-1}$).

### 4.2.3 The Role of the Genomic DNA in the Force-Driven Transitions

To explore the importance of the genomic DNA in the stepwise transitions we carried out fatigue experiments on emptied particles.

First, we treated the particles at 65 ˚C for 15 minutes to release their DNA and then indented them with 1.5 nN maximal force in repeated cycles similarly as in the measurement at room temperature. Here we also observed repeatable indentation force traces, however the number of the indentation prior to the capsid failure was significantly lower than at room temperature. **Fig. 22.a** shows that the capsid collapsed after only 15 indentations compared with 96 at room temperature, which indicates that the DNA indeed contributes to the mechanical stability of the phage particles and increases the resilience against the mechanical fatigue of the capsids. However, the indentation curves similarly contained discrete step-like transitions which show remarkably similar appearance to those observed in the room-temperature phage particles (**Fig. 22.a**). We performed the same distance step size analysis as previously and found that the distribution is also multimodal (**Fig. 22.b**). The peaks at 0.59 nm (± 0.37 nm) and 1.24 nm (± 0.26 nm) correspond well to the first and second peaks of the room temperature control, at integer multiples of the ~0.6 nm unit step

size. However, an additional peak appeared at 0.29 nm (±0.19 nm), which is one-half of the unit step size.
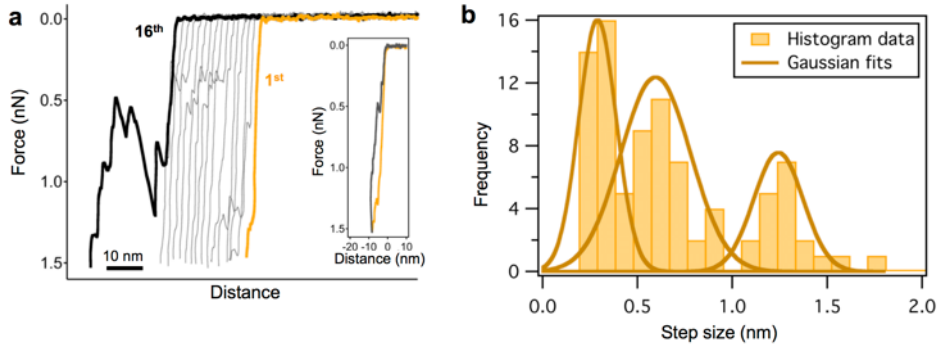


**Fig. 22.** Discrete nanoindentation steps in heat-treated (65 ˚C) T7 bacteriophage capsids. (**a**) Force versus distance curves collected in 16 consecutive nanoindentation experiments on the same capsid. The curves were shifted along the distance axis with 1 nm to better display changes in transition positions. The maximal indentation force was limited to 1.5 nN throughout the experiment. (**b**) Distribution of the transition step size. Gaussian were fitted on the cumulative step-size dataset. The peaks are centered at 0.29 (±0.09), 0.59 (±0.19) and 1.24 (±0.13) nm.

## 4.3 Mechanically-Driven DNA Ejection of the Bacteriophage T7

### 4.3.1 Mechanically-Triggered DNA Ejection

We previously observed in our measurements that the DNA can occasionally release from the capsid during the AFM scanning (**Fig. 15.b**). Therefore, we decided to explore the role of the mechanical force exerted by the tip on the capsid in triggering DNA ejection. To visualize the topographical structure and mechanically-induced changes of the phage particles, we covalently attached them to the surface as previously (see in **Materials and methods**) and scanned them with low exerted force (**Fig. 23.**). In these images, we were able to resolve the tail of the phages, which appeared as a cone with a mean length of 22.8 nm (±3.0 nm SD, n=149). The tail lengths were determined by analyzing the height cross-sectional profile of the capsids (**Fig. 23.b**) and the measured mean length compared well with previously reported data (23nm[95]).
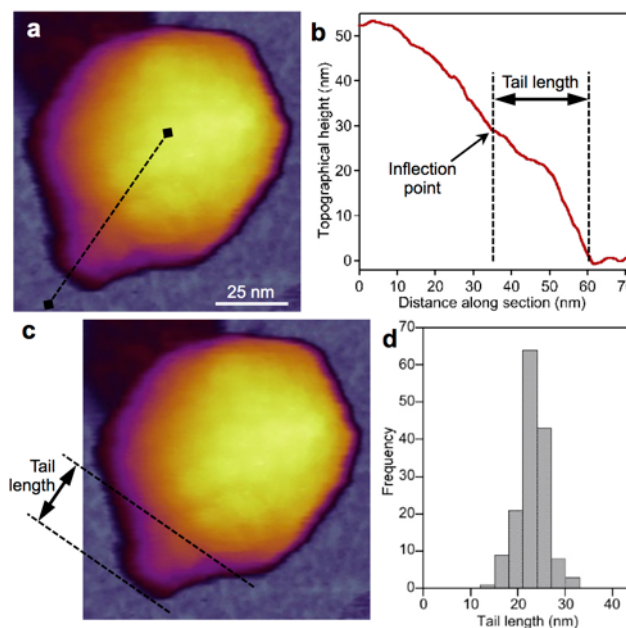
**Fig. 23.** Measurement of the T7 phage tail length. (**a**) Height-contrast AFM image of a T7 phage. The dotted line marks the linear section along which topographical height data were collected. (**b**) Topographical height as a function of distance along the linear section. (**c**) The calculated tail-length projected onto the AFM image. (**d**) Distribution of the calculated tail lengths.

During the scanning, the DNA suddenly became visible as the tip passed through the capsids (**Fig. 24.**). The DNA strands appeared as random threads bound to GD-mica and emerged abruptly from one scan line to the next. This suggests that the DNA may be released by the mechanical tapping of the capsid by the cantilever tip. The ejected DNA was particularly well resolvable in phase-contrast AFM images due to the differences in the viscoelastic properties of DNA and the mica substrate (**Fig. 24.c. and d.).**
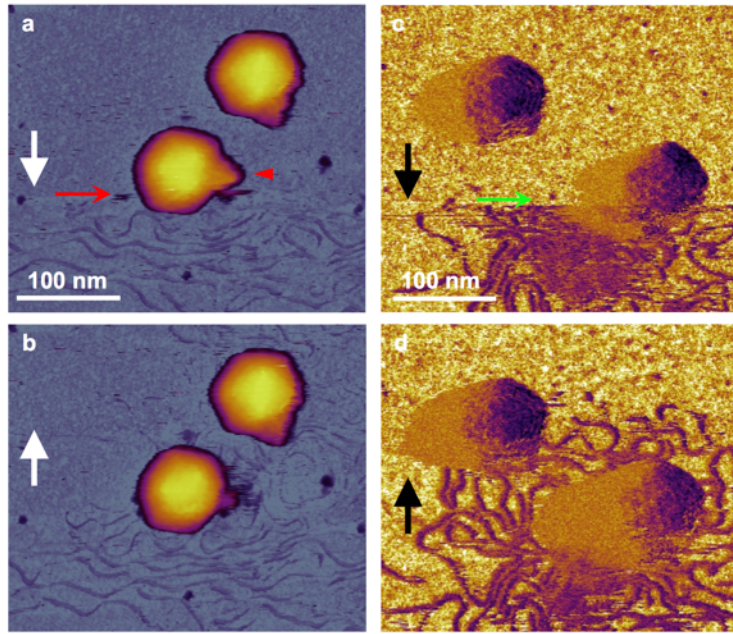
**Fig. 24.** *In situ* AFM of DNA ejection from the T7 bacteriophage. (**a-b**) Sequential height-contrast AFM images collected during (**a**) and following (**b**) DNA ejection. Collection of the two images was separated by 7 minutes. White arrows indicate AFM line-scanning direction. Red arrow points at the scan line in which DNA suddenly appeared, while the red arrowhead points at the tail complex, the surface of which became fuzzy after DNA ejection. (**c-d**) Sequential phase-contrast AFM images collected during (**c**) and following (**d**) DNA ejection. Images are separated by 8 minutes. Black arrows indicate AFM line-scanning direction. Green arrow points at the scan line in which DNA suddenly appeared in the image.

To explore the details of DNA ejection further, we performed additional in situ AFM measurements by scanning the same capsids continuously as a function of time (**Fig. 25.**).
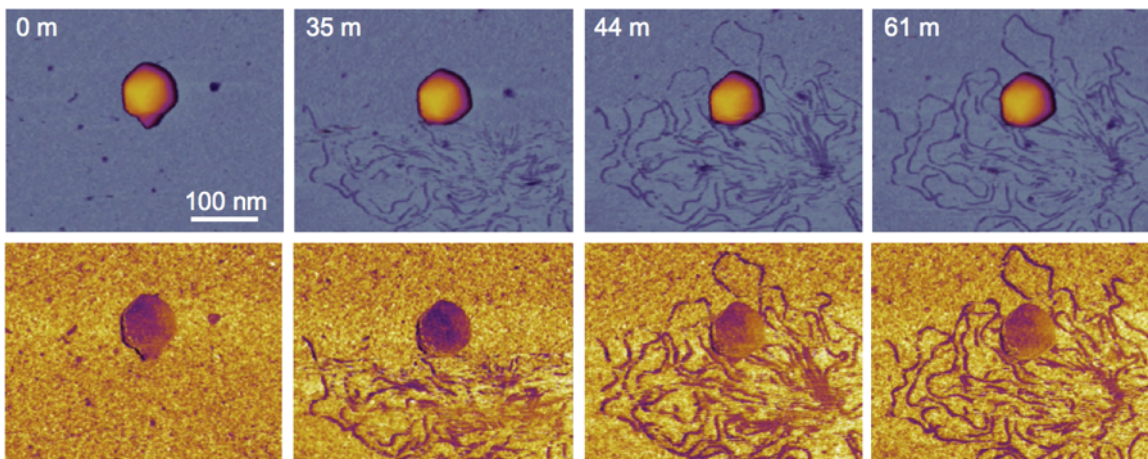


**Fig. 25.** *In situ* AFM of mechanically-triggered DNA ejection. Height-contrast AFM images are with gray background and annotation indicating the collection time of the frame in minutes. Phase-contrast AFM images of the same T7 particle are with orange background. Frame size is 450 nm x 450 nm.

Based on the high-resolution time-dependent AFM images we were able to explore several key features of the mechanically-driven DNA ejection process:

1. The ejected and surface-adsorbed DNA was presumably only a partial T7 genome in a kinetically trapped structural state. To validate this hypothesis, we compared the size of the area covered by ejected DNA in the AFM images with that computed from the total length of surface-equilibrated and surface-projected T7 DNA genome.

2. The DNA ejection visibly occurred via the tail complex (**Fig. 24.**), indicating that the process took place forcibly through its natural path. To determine whether the DNA was ejected due to the cantilever tip breaking off the tail, we performed additional measurements, where the DNA ejection was triggered while tapping the body of the capsid without touching the tail.

3. The DNA ejection occurred via the tail complex at a certain rate specific to T7 phage. We estimated this rate by analyzing sets of consecutively scanned images and compared it with results measured earlier.

4. The mechanical load exerted further away from the tail complex causes perturbation that propagates through the compressible medium of the DNA-filled capsid eventually triggering the DNA ejection. We estimated the internal pressure increment that was generated due to cantilever oscillation and led to DNA ejection.

Further details with the topographical analysis of the images and the corresponding calculations are presented in the **Discussion** section.

4.3.2 The Effect of Increased Mechanical Load on the DNA Ejection Triggering Rate

To directly verify the role of force in triggering DNA-ejection and characterize its energetic topology, we exposed T7 capsids to increasing average mechanical load and measured the ratio of DNA-ejected particles (**Fig. 26.**).
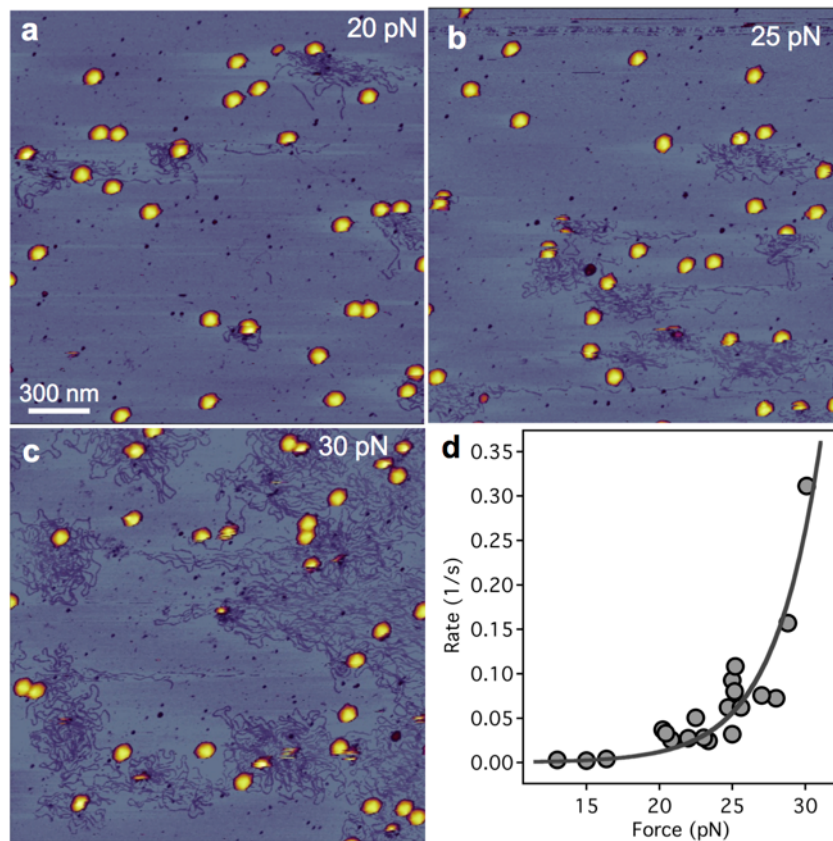
**Fig. 26**. The effect of increasing mechanical load on the DNA ejection triggering rate. 2 x 2 μm AFM images of the same sample exposed to an average (**a**) 20 pN, (**b**) 25 pN and (**c**) 30 pN load. (**d**) Rate of DNA ejection as a function of mechanical load. Data were fitted with equation (5.11)

We scanned different large areas (2x2 μm) of the same sample with gradually increasing forces, which resulted in progressively more ejected DNA appearing on the surface.

Further analyzing the AFM images of the DNA ejected T7 capsids, we also found that the DNA was highly unevenly distributed around the particles indicating that the ejection process generates a local propulsion, which transfers the expelled molecule across the viscous medium. Although, significant internal pressure is evidently present inside the T7 capsid, the role of it is unclear because the T7 DNA ejection into the host is strongly attributed to enzymatic mechanisms[96]. In the AFM images, we also observed globular particles directly near the ejected DNA with an average height of 5.0 nm (±1.5 nm SD, n=81) (**Fig. 27.**). We speculate that they may correspond to the viral core proteins gp14, gp15 and gp16, which are ejected prior to DNA and might contribute to the ejection conduit[95,97].
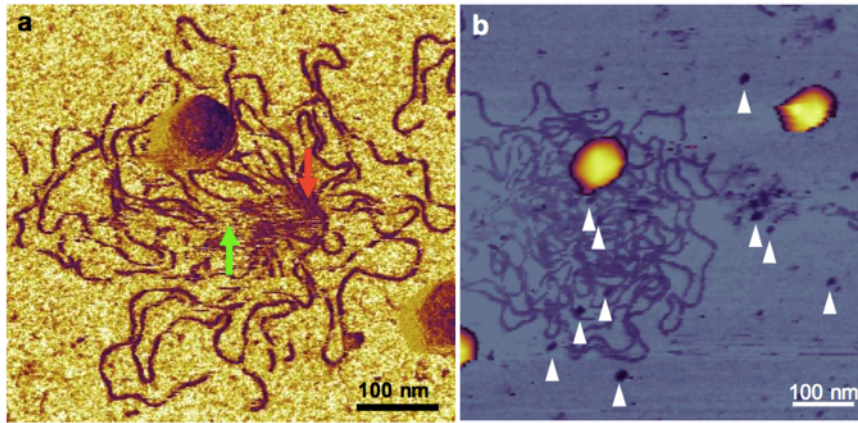
**Fig. 27.** Analysis of viral material ejected upon mechanical trigger. (**a**) Phase-contrast AFM image of the ejected and surface-adsorbed genomic DNA. Green and red arrows point at the center of DNA mass and the maximum of DNA density, respectively. (**b**) Globular particles (marked by white arrowheads) in the vicinity of the ejected DNA molecule.

### 4.3.3    The Effect of Chemical Fixation on DNA Ejection

To explore the possible mechanisms behind the switch-like triggering of the DNA-ejection, we chemically fixed the surface attached particles with 5% glutaraldehyde (**Fig. 28.**). Before the fixation, the particles were covalently bound to the surface, similarly as in our previous experiments (GD-mica, see details in **Materials and methods**). We anticipated that such a fixation step would completely abolish DNA ejection because of the structural stabilization of the capsid wall. Surprisingly, the mica surface was already covered with DNA by the time the AFM scanning started, indicating that the fixation facilitated enhanced triggering of DNA ejection (**Fig. 28.a**). Furthermore, the tail fibers of the T7 phages became visible on the capsid surface due to the fixation (**Fig. 28.b**). This suggests that the surface immobilization of the tail fibers triggered DNA ejection, similarly to the previously described mechanical loading (**Fig. 28.c**).
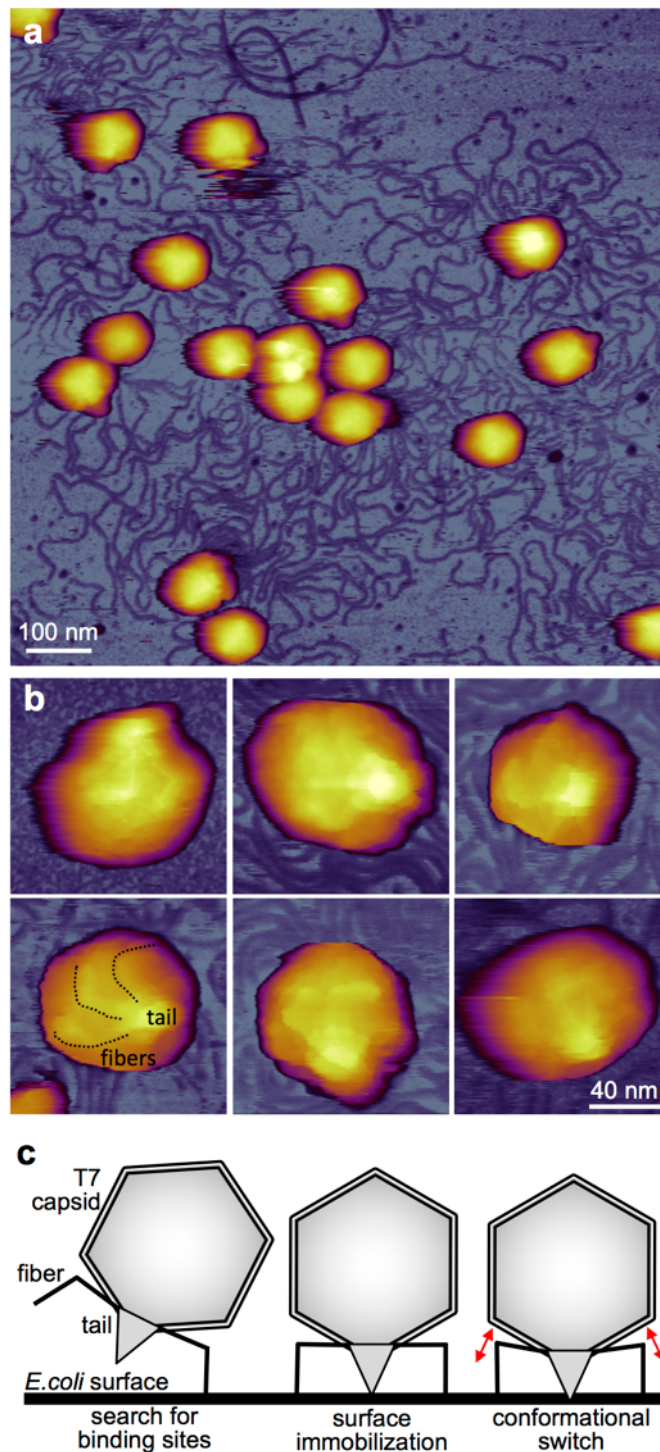
**Fig. 28.** Chemical fixation of T7 phage particles. (**a**) AFM image of surface attached T7 phage particles fixated with glutaraldehyde. (**b**) AFM images of individual T7 particles with their tail complex pointing away from the substrate surface. Dotted lines in the bottom left image denote the fibers immobilized on the capsid surface (**c**) Schematic model of T7 binding to the *E. coli* surface and passing through a switching step prior to genomic DNA release. Red double arrows indicate the putative conformational switch thought to be associated with a change in the fiber arrangement.

# 5   DISCUSSION

## 5.1   Thermally-Induced Structural Changes in Bacteriophage T7

### 5.1.1   Analysis of the Heat-Induced Topographical Changes

To reveal the structural details and mechanisms behind the heat-induced mechanical changes in T7 bacteriophages, we performed high-resolution AFM imaging and indentation experiments on particles that were exposed to 65 ˚C and 80 ˚C (**Fig. 16**, **Fig. 17**).

To quantify the heat induced structural changes of the T7 particles, we analyzed the cross-sectional height profile of different features in the images. Representative height profiles across the center of individual capsids demonstrate the topographical differences of T7 phages treated at various temperatures (**Fig. 29.a**).
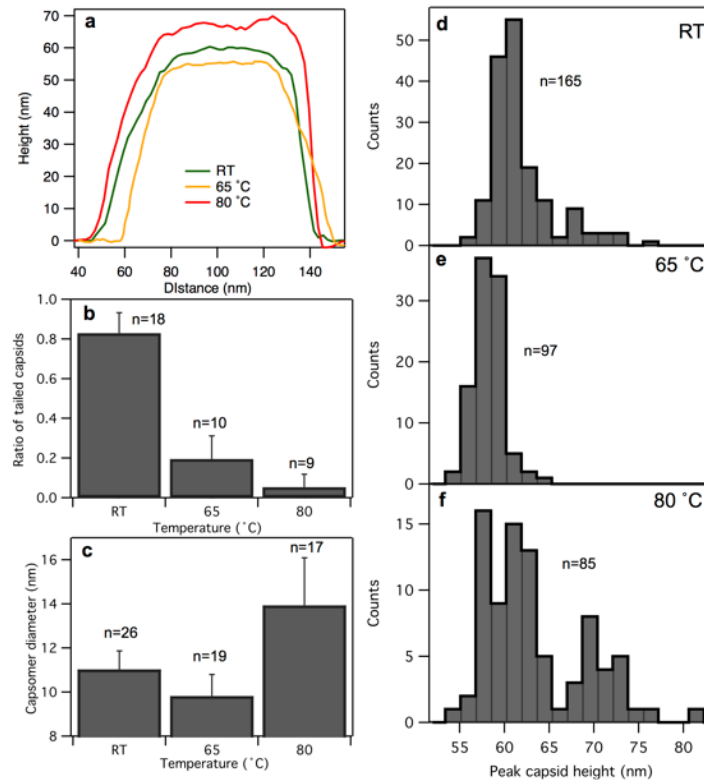


**Fig. 29.** Analysis of capsid topography data. (**a**) Topographical height map along the cross-section of either a capsid at room temperature (green trace) or ones treated at 65 ˚C (orange) or 80 ˚C (red). (**b**) Ratio of capsids with tails as a function of temperature. The numbers above the bars represent the number of fields analyzed for every T7 particle. Error bars represent standard deviation (SD). (**c**) Capsomer diameter as a function of temperature. The numbers above the bars represent the number of capsomers measured. Error bars represent standard deviation (SD). (**d**) (**e**) and (**f**) show histograms of peak capsid heights for room-temperature (RT), 65 ˚C and 80 ˚C treated T7 phages, respectively. Peak height refers to the tallest topographical point in the capsid image. The numbers (n) refer to the number of T7 phage particles analyzed.

The 65 °C treatment led to the capsid shrink slightly, its faces got flattened while its edges more pronounced. By contrast, the 80 °C treated capsid became swollen and its surface rugged. We also found that the number of capsids with visible tail complex progressively reduced upon heat treatment (**Fig. 29.b**). Furthermore, the average diameter of the capsomers increased considerably upon 80 °C treatment (**Fig. 29.c**). We hypothesize that this increase in the apparent volume was caused by some thermally-induced conformational changes, most likely partial denaturation that occurred in the gp10A capsomeric proteins. It is possible that the partial denaturation exposed the hydrophobic core of the capsomer proteins, and a hydrophobic interaction occurred in between neighboring capsomers. The peak capsid height decreased slightly upon 65 °C treatment (**Fig. 29.d-e**) but the 80 °C treatment resulted in the emergence of a sub-population with larger height values (**Fig. 29.f**). This sub-population may correspond to the particles with swollen wall structure.

Finally, we analyzed the globular particles after the different treatments. Their number progressively increased per field with the temperature of the treatment (**Fig. 30.a**). The typical height of the particles was similar, centered around 6 nm regardless of heat-treatment (**Fig. 30.b-d**). However, in case of the 80 °C treated sample a population with larger particle heights emerged (**Fig. 30.d**). We speculated that the ~6 nm particles may correspond to the ejected core proteins, while the large globular particles are most likely the aggregates of capsomeric proteins that developed due to the complete disassembly of some capsids.
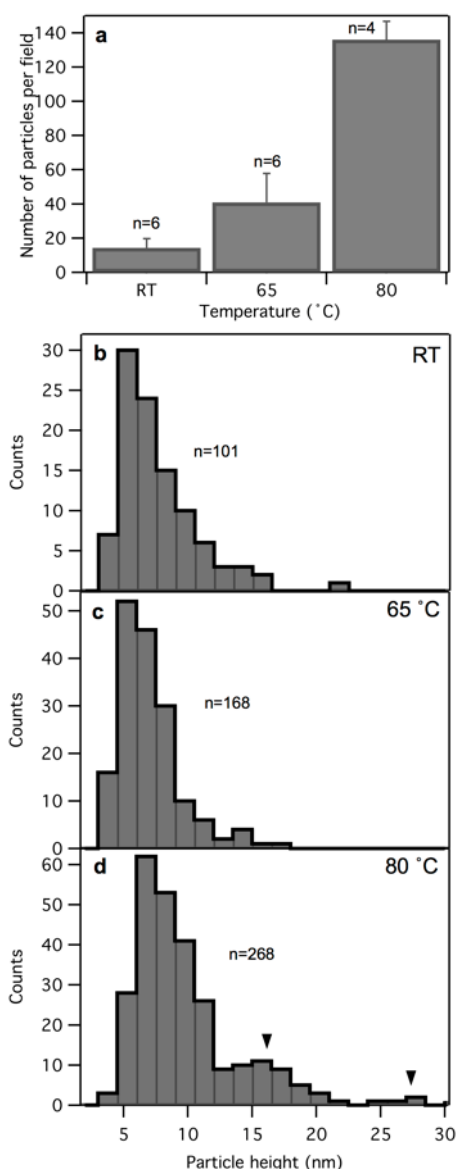
**Fig. 30.** Topographical analysis of globular particles. (**a**) Number of globular particles per field as a function of temperature. The numbers above the bars represent the number of fields analyzed for every particle. Error bars represent standard deviation (SD). (**b**) (**c**) and (**d**) show histograms of the globular particle height for samples at room temperature (RT) and ones treated at 65 ˚C and 80 ˚C, respectively. Black arrowheads point at populations of large globular particles. The numbers (n) refer to the number of globular particles analyzed.

### 5.1.2 Analysis of the Heat-Induced Nanomechanical Changes

Following the topographical exploration of the heat-treated particles, we performed indentation experiments with AFM to reveal the thermally-induced changes in their nanomechanical properties. We further derived and analyzed several parameters of the force curves, the histograms of which are shown in **Fig. 32**. The distribution of breaking force values of the RT particles in **Fig. 29.a** naturally divide into two modes, according to the

45

distinct types of force curves found in **Fig. 18.c-d**. Since the first peak of the breaking force histogram for the RT samples aligns well with the single peak for the 65 ˚C samples, and the T7 phages heated above 60 ˚C are expected to lose their DNA[8,90–94], we concluded that this peak corresponds to empty capsids. The breaking force was significantly reduced in case of the 65 ˚C-treated capsids (from 6.80 nN to 1.61 nN, see **Table 1**), indicating that the presence of packaged DNA within the phage contributes considerably to its mechanical stability. Interestingly, the breaking force was increased for the 80 ˚C-treated particles. This might be explained by structural rearrangements between the capsomeric proteins that occurred between 65-80 ˚C, which stabilized their interactions and led to an increased overall mechanical stability of the phage particle.
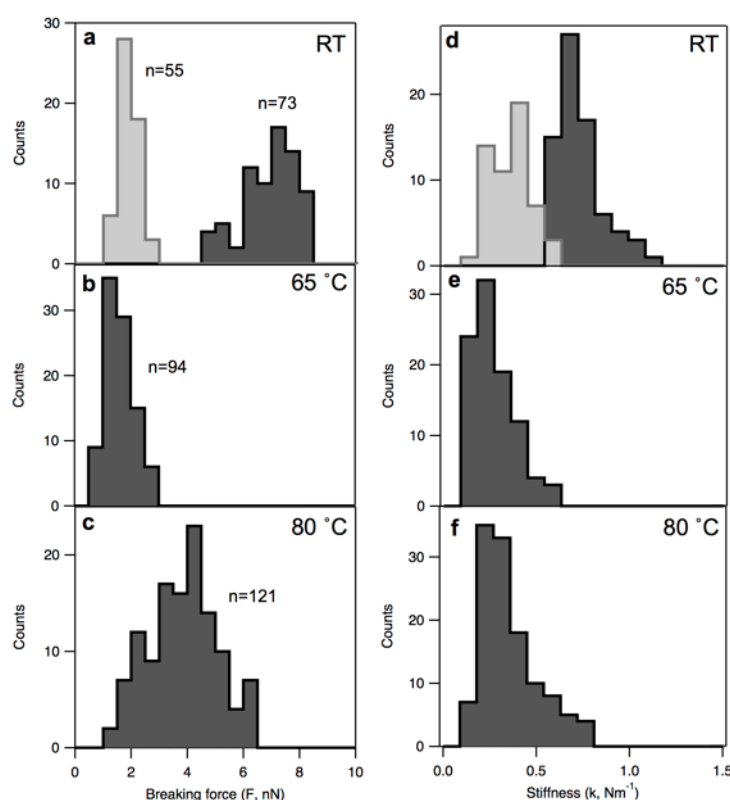


**Fig. 31.** Distribution of breaking force (**a, b, c**) and stiffness (**d, e, f**) parameters for T7 phage particles at room temperature (RT) and ones exposed to 65 ˚C and 80 ˚C temperatures, respectively. Light gray bars correspond to data obtained on empty capsids at RT. The numbers (n) refer to the number of force curves analyzed to obtain the nanomechanical parameters.

The calculated stiffness was twice as large in case of the intact T7 phages, then for the empty RT capsids and the heat-treated ones (**Fig. 31.d-f, Table 1**). This suggest that the presence of packaged DNA contributes to the stiffness of the T7 phage.

The maximal indentation value progressively increased with the heat-treatments, as a combined effect of the underlying changes in breaking forces and stiffness (**Fig. 32.a-c, Table 1**). The mean capsid height slightly reduced due to the 65 ˚C treatment (**Fig. 32.d-f, Table 1**Error! Reference source not found.), essentially identical to that of the empty RT capsids, indicating that the packaged DNA increases the capsid diameter by approximately 1 nm. The capsid height distribution of the 80 ˚C-treated samples had a slightly increased mean (**Fig. 32.f, Table 1**), which was probably caused by the emergence of a larger-diameter capsid subpopulation.
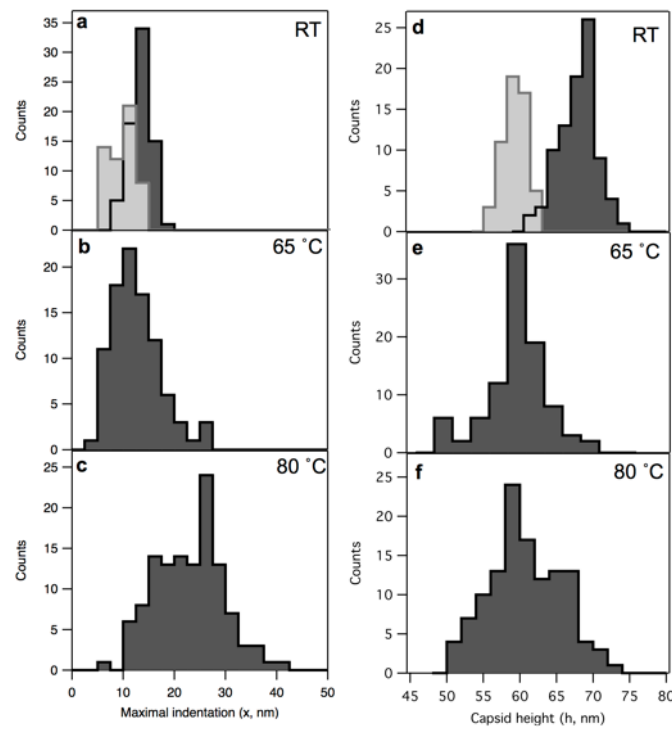


**Fig. 32.** Distribution of maximal indentation distance (**a, b, c**) and capsid height (**d, e, f**) parameters for T7 phage particles at room temperature (RT) and ones exposed to 65 ˚C and 80 ˚C temperatures, respectively. Light gray bars correspond to data obtained on empty capsids at RT.

**Table 1.** Summary of nanomechanical and topographical parameters of T7 bacteriophage capsids and globular particles.

| | RT (DNA-filled) | RT (empty) | 65 °C | 80 °C |
|---|---|---|---|---|
| Nanomechanics parameters | | | | |
| Breaking force ($F$, nN) | 6.90 ± 0.97 | 1.90 ± 0.34 | 1.61 ± 0.52 | 3.83 ± 1.20 |
| Capsid stiffness ($k$, Nm$^{-1}$) | 0.73 ± 0.12 | 0.36 ± 0.10 | 0.27 ± 0.11 | 0.35 ± 0.15 |
| Maximal indentation ($x$, nm) | 13.24 ± 2.13 | 9.51 ± 2.41 | 12.56 ± 4.70 | 22.97 ± 6.61 |
| Capsid height ($h$, nm) | 60.4 ± 1.71 | 59.93 ± 1.56 | 59.41 ± 4.00 | 60.71 ± 4.87 |
| Capsid topographical parameters | | | | |
| Ratio of tailed capsids | 0.83 ± 0.1 | NA | 0.19 ± 0.12 | 0.05 ± 0.06 |
| Peak capsid height (nm) | 61.8 ± 3.6 | NA | 58.2 ± 1.7 | 63.3 ± 5.5 |
| Capsomer diameter (nm) | 11.0 ± 0.8 | NA | 9.8 ± 1.0 | 13.9 ± 2.2 |
| Globular particle parameters | | | | |
| Particle height (nm) | 7.6 ± 3.2 | NA | 6.9 ± 2.5 | 10.0 ± 5.4 |

### 5.1.3 The Model of Thermally-Induced Structural Changes in Bacteriophage T7

Following the analysis of these measurements, we constructed a phenological model to further interpret the results (**Fig. 33.**).

According to our model, at room temperature the T7 particles shows icosahedral structure with distinctive tail complex. Due to the internal DNA pressure, the capsid is slightly swollen and stiff, therefore it is able to withstand instantaneous forces up to 8 nN prior to breakage (**Fig. 33.a**)
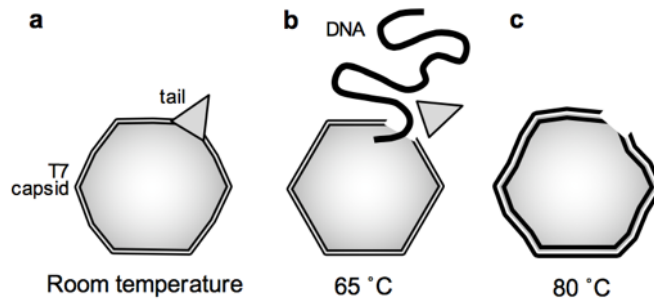


**Fig. 33.** Schematic model of thermally-induced changes in the T7 bacteriophage. (**a**) At room temperature, the capsid is slightly swollen because of the DNA pressure inside. The bulging of the capsid wall as shown in the scheme is not to scale. (**b**) Upon heating to and incubating at a temperature of 65 °C, the tail complex breaks off, resulting in the release of the genomic DNA. The capsid becomes more faceted due to the decrease of the capsid pressure. (**c**) Finally, at 80 °C the capsid becomes swollen and its surface irregular, and the capsids may become fragmented into large globular particles (this last step is not shown).

In case of a 65 °C treatment, the DNA gets ejected from the capsid due to the abruption of the conical tail complex (**Fig. 33.b**). During natural DNA ejection only a part of the DNA is driven out from the capsid due to the DNA pressure, the remaining part may be pulled

out into the *E.coli* by an active process[95,98,99]. However, in case of the thermal-treatment, the abruption of the tail complex gives way to the releasing of the entire T7 genome, although the exact length of the DNA section that exits from the capsid is still uncharacterized. Regardless of the ejected DNA length, the DNA pressure drops off, which leads to a slight shrinkage and therefore a more faceted appearance of the capsid.

Upon further heating the particles to 80 ˚C, their global structure is still maintained (**Fig. 33.c**). A partial denaturation likely takes place in the gp10A proteins of the capsid wall, which leads to the exposure of the hydrophobic protein regions. These processes result in capsomer swelling and a new set of inter-capsomeric interactions. In the end, the capsid wall becomes thicker and its entire surface rugged. Many of the capsids are likely to completely disassemble, as evidenced by the presence of large aggregates of globular particles. For the capsids that do not completely fall apart during the 80 ˚C treatment, the breaking force is increased, which may be the result of the stabilization of the hydrophobic interaction upon cooling back to RT. Therefore, the capsid stabilization may not be the direct result of the heating per se, rather that of the relaxation from the thermal exposure.


## 5.2    Stepwise Reversible Buckling of Bacteriophage T7

### 5.2.1    Nanomechanical Buckling of Bacteriophage T7

Applying load repeatedly with low maximal force we performed fatigue experiments on DNA-filled capsids. One-fifth of the indentation force traces contained multiple discrete, step-wise transitions. The distribution analysis of the transition step-sizes showed peaks at integer multiples of approximately 0.6 nm (0.58 nm ± 0.21, SD) These data suggest that a single transition corresponds to a ~0.6 nm shift of the capsid structure. We concluded that this shift might correspond to a slight, discrete structural change closely related to the capsomers. During the T7 capsid maturation, the capsid wall expands while the gp10 N-terminal segment swings to the capsid surface. It is possible that the observed transition step is related to a force-driven backwards step along the structurally stabilizing maturation pathway. The fifth peak of the histogram corresponds to the largest step size with 2.92 nm (±0.19, SD) which is five times larger than the 0.6 nm individual step size. This suggests that the largest step is the sum of five individual steps. The last indentation curve of the fatigue experiment, obtained just prior to the complete capsid collapse, contained five

transitions implying that one stepwise transition corresponds to a unit structural failure that lowers the capsid stability, and the accumulation of five such failures leads to complete structural collapse.

We speculate that the structural failure is associated with the pentameric capsomer for three reasons: (a) the probability of observing stepwise transitions in the force traces was approximately 0.2, which compares well with the ratio of pentamers (12) to hexamers (60) covering the capsid surface; (b) the maximum number of steps leading to capsid collapse is five; and (c) because the T7 virion is faceted, the pentamers protrude from the capsid surface, making them mechanically accessible and prone to buckling. Therefore, it is likely that we observe step-like transitions when a pentamer of the T7 capsid points upward, in 5-fold symmetric orientation. Accordingly, if five structural failures are accumulated by a pentamer, it is no longer able to withstand the pressure exerted by the cantilever and allows the AFM tip to penetrate the capsid. However, if the pressure is relieved prior to the complete collapse, then the capsid structure is able to rapidly reconcile.

### 5.2.2 Energetic Topology of the Mechanically-Driven Transitions

To estimate the energetic topology of the mechanically-driven transitions, we performed dynamic force spectroscopy experiments using different loading rates in the range of 0.1 to 5 μm/s (**Fig. 21.b**). We calculated the loading rate, the instantaneous change in the loading force in the moment of the induced structural transition, for each transition of the reversible nanoindentations. The loading rates were determined by finding the slope ($r=\Delta F/\Delta t$) of the force versus time curve just prior the buckling transition either in the forward (indentation) or reverse (relaxation) direction (**Fig. 34.**).
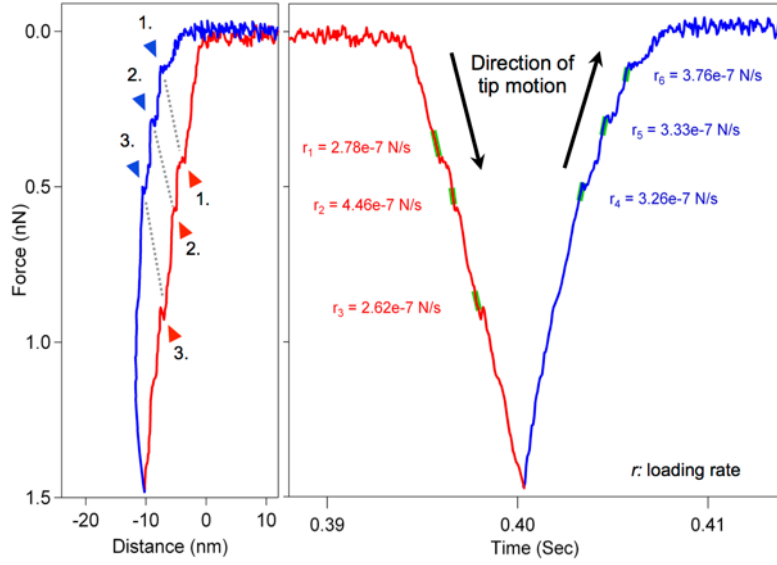
**Fig. 34.** Loading rate measurement of buckling transitions. Left, the first, second and third buckling transitions (labeled 1, 2 and 3) identified on the indentation force trace were matched with their corresponding reverse transitions on the retraction curve. Right, loading rates were measured on the force versus time traces independently for both the indentation and retraction traces as the slope of trace just prior the transition (green lines).

For dynamic force spectroscopy analysis, we considered the transition force versus calculated loading rate data of the first three transitions separately for both the forward and reverse direction (**Fig. 35.**). The transition force ($F_t$) *versus* loading rate ($r$) data were smoothed with the Savitzky-Golay filter (35-point window), then fitted with equation

$$F_t = \frac{k_B T}{x_\kappa} ln\left(\frac{r x_\kappa}{k_{off} k_B T}\right) \tag{5.1}$$

where $x_\kappa$ is the distance between the starting structural state and the transition state along the reaction coordinate, $k_{off}$ is the spontaneous reaction rate in thermal equilibrium, and $k_B T$ is thermal energy[100].
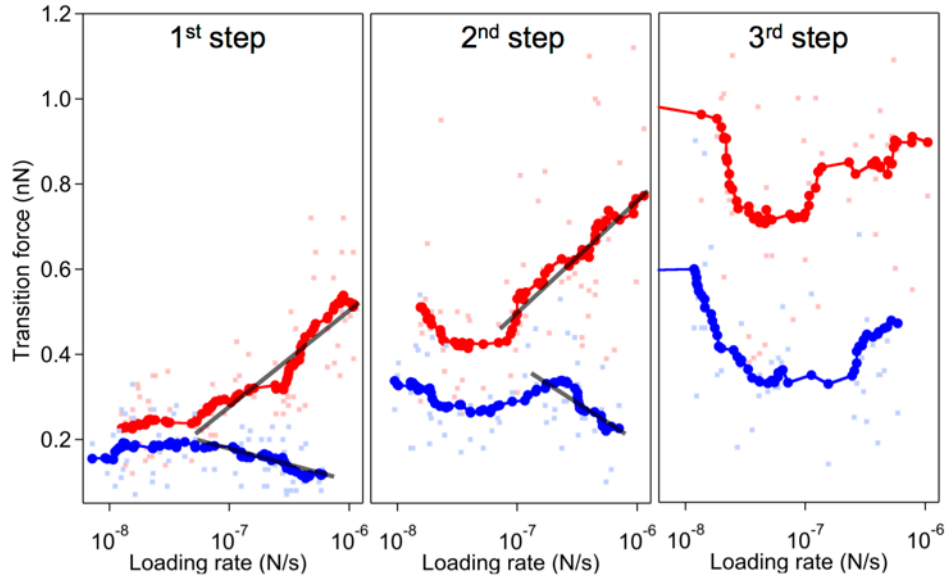
**Fig. 35.** Dynamic force spectroscopy of T7 bacteriophage capsids at room temperature. Transition forces as a function of loading rate during the forward (buckling, red) and reverse (relaxation, blue) transitions are shown for first, second and third steps.

While we were able to properly fit the data for the first two transitions, the smaller sample size and the large scatter of the third transition prevented a reliable analysis. The calculated values for transition distance $x_K$ and spontaneous rate $k_{off}$ are shown in **Table 2**.

**Table 2.** Coefficients obtained by fitting the dynamic force spectroscopy data.

|  | Transition distance ($x_K$) | Spontaneous rate ($k_{off}$) |
| --- | --- | --- |
| First step forward (buckling) | 0.4 Å | 52 s$^{-1}$ |
| First step reverse (relaxation) | 1 Å | 7×10$^5$ s$^{-1}$ |
| Second step forward (buckling) | 0.4 Å | 10 s$^{-1}$ |
| Second step reverse (relaxation) | 0.5 Å | 2×10$^5$ s$^{-1}$ |

We concluded that a small structural disruption is sufficient to reach the transition state during indentation, but a larger structural rearrangement is required during consolidation. Furthermore, the consolidation reaction proceeds orders of magnitudes faster under thermal equilibrium than spontaneous disassembly, indicating that the structural consolidation process is strongly biased forward. A similar ratio of the forward and reverse reactions was found in the case of the second transition.

### 5.2.3  The Role of the Genomic DNA in Force-Driven Transitions

To explore the role of genomic DNA in the force-driven transitions we performed fatigue experiments on emptied capsids, where we removed the DNA by heat treating the particles

at 65 ˚C. The indentation was still repeatable on the DNA-emptied capsids but they collapsed sooner, after at most 15 subsequent cycles. The indentation curves also contained discrete step-like transitions with the peaks of the distance step sizes at integer multiples of the ~0.6 nm well aligning with those of the DNA-filled capsid, plus an additional peak at ~0.3 nm.

Based on our findings we concluded that the force-driven transitions are restricted to structural rearrangements within the proteinaceous capsid only, and are independent of the dsDNA content. In addition to the fewer indentations required for the collapse, we also found fewer stepwise transitions in the traces, which suggests that the structural stability of the capsid decreased due to the heat treatment. The observed fractional step also indicates development of structural changes within the capsomeric proteins that contribute to mechanical weakening. Such a partially weakened capsid architecture is likely to contribute to the more pronounced fatigue and the smaller breaking forces of the heat-treated samples.

### 5.2.4   Phenomenological Model of the Mechanically Induced Stepwise Buckling

The fatigue and dynamic force spectroscopy experiments described in the previous sections revealed that the discrete, stepwise transitions appearing in the force distance curves are related to certain force-driven changes in the proteinaceous capsid shell.

The fatigue measurements showed that these stepwise transitions are related to the pentameric unit of the capsid and it is also known that the mechanical forces cause elastic deformations and buckling in spherical shells[51,101–110]. Therefore, we speculate that the stepwise transitions are related to the buckling of the capsid pentameric unit. To correlate the unit buckling amplitude, the 0.6 nm individual step size, with the structural features of the T7 capsid we proposed a simple geometric model.

Since the pentamer protrudes from the capsid surface, we speculate that buckling is initiated at or near one of the corners of the pentamer. Upon increasing the load on one such pentameric corner, the blue contour marked convex triangular pyramid inverses and becomes concave by chiral symmetry (**Fig. 36**). Twice the height of this pyramid provides a geometrical estimate of the buckling step size. Using simple trigonometry this height is about 0.2 times the capsomeric edge length of the T7 phage, which is around 7-8 nm. This suggests an overall buckling amplitude of ~3 nm, which is five times greater than the measured 0.6 nm individual step size of the transitions. Thus, the unit buckling step involves

a structural transition that occurs along a fraction of the edge. According to this model, with increasing mechanical load on the protruding pyramidal corner, the buckling may not run along the entire edge of the capsomer but only a small fraction of it, which is possibly only a part of the underlying gp10A protein.
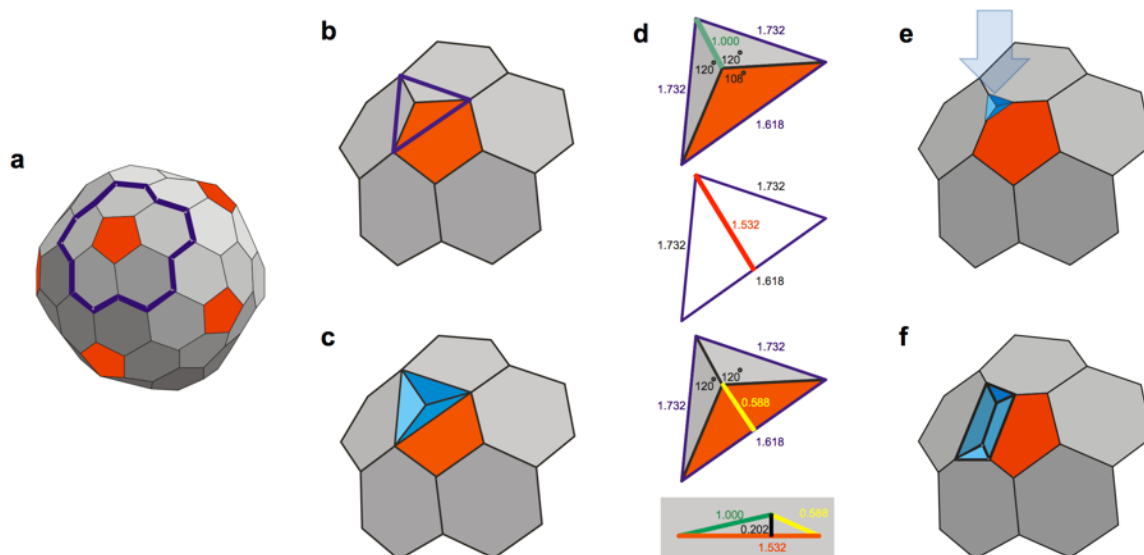


**Fig. 36.** Phenomenological model of the mechanically induced stepwise buckling of the T7 capsid. (**a**) Schematics of the T7 capsid with the involved group of capsomers (a pentamer with the surrounding hexamers) outlined (thick blue line). Outline of the protruding pyramid on the capsid surface in the relaxed (**b**) and buckled (**c**) configuration. (**d**) Trigonometrical analysis of the buckling step size. The height of the convex pyramid is 0.2 times the length of the edge (bottom figure) according to simple triangle height calculations. (**e**) The first buckling step induced by indentation with the AFM cantilever (blue arrow). (**f**) Progression of buckling along the capsid surface.

During the subsequent stepwise transitions, the buckling progresses along the capsid surface towards the other corners of the pentamer. The molecular mechanism behind the buckling phenomenology is probably more complex than this simple geometric model and is likely to involve intra- or intermolecular changes within or between the component gp10A capsomeric proteins. Cryo-EM measurements describe the structural basis of maturation-dependent inter-capsomeric interactions[18], but the details of the structural rearrangements during maturation are still unknown. The linkage between the capsomers is accomplished by the interaction of an N-terminal hairpin-like loop and an A-pocket of its neighbor[18]. The final maturation step starts with the transient unfolding of the gp10A N-terminal helix,

which swings through the capsid shell, then forms and consolidates the intercapsomeric linkage.

We speculated that the stepwise transitions observed in our indentation experiments may be associated with the transient rupture or shifting of the inter-capsomeric linkages. Furthermore, the reverse steps observed during cantilever retraction may correspond to the re-formation of the intercapsomeric linkages and thereby to the final capsid maturation step.

### 5.2.5  Kinetics of Force-Driven Transitions

To obtain deeper insight into the kinetics and thermodynamics of the buckling process, we further analyzed the dynamic force spectroscopy results (**Fig. 35.**). Previously we concluded that the structural consolidation process is highly biased forward and proceeds at a spontaneous rate of $7 \times 10^5$ s$^{-1}$ under mechanically unloaded conditions. If we assume that the ~0.6 nm transitions are the mechanical manifestations of the final capsid maturation step and the intercapsomeric joints are established sequentially, the complete maturation of one T7 phage particle occurs in little below 1 ms at this $7 \times 10^5$ s$^{-1}$ rate.

Although the maturation step is strongly forward-biased, the mechanical force may sufficiently decelerate this reaction during cantilever retraction and accelerate the reverse step by indentation, so that an apparent equilibrium is established. Such an apparent equilibrium is observed for the first indentation and retraction steps at approximately 200 pN (**Fig. 21.**). Because of the equilibrium, the free-energy change of the maturation step may be estimated from the mechanical work[111]. The 0.6 nm step at 200 pN corresponds to a free-energy change of 72 kJ mol$^{-1}$. By comparison, a free-energy change of ~55 kJ mol$^{-1}$ has been calculated for the final maturation step of the HK97 capsid in DSC experiments[112]. These two are in good agreement, considering that part of the work performed by the cantilever is invested in the elastic deformation of the capsid.

Our findings indicate that the equilibrium structure of the T7 phage is highly dynamic, which may be important in protecting the genomic DNA and making the capsid structure resilient even under harsh environmental conditions.

## 5.3 DNA Ejection Triggered by a Sensitive Mechanical Switch

### 5.3.1 The Role of Mechanical Force in Triggering DNA Ejection

We investigated the role of mechanical force in triggering DNA injection by visualizing the topographical structure and mechanically-induced changes of T7 phages. We scanned individual surface attached capsids continuously as a function of time, where the DNA released from the capsids in response to the mechanical tapping of the cantilever tip, then analyzed the images to explore several key features in-depth.

First, we hypothesized that the ejected and surface-adsorbed DNA was only a partial T7 genome in a kinetically trapped structural state. We compared the size of the area covered by ejected DNA in the AFM images with that computed from the total length of surface-equilibrated and surface-projected T7 DNA genome.

The mean diameter of the areas covered with the ejected DNA around the individual capsids was measured 355 nm (±57 nm SD, n=43). As a comparison, we estimated the area occupied by the full-length T7 dsDNA in surface-equilibrated and in surface-projected condition, where the polymer chain is driven to the surface.

The mean-square end-to-end dsDNA distance of a statistical polymer chain equilibrated to a substrate surface can be calculated as[113]

$$\langle R^2 \rangle_{2D} = 4L_P L_C \left( 1 - \frac{2L_P}{L_C} \left( 1 - e^{-\frac{L_C}{2L_P}} \right) \right) \tag{5.2}$$

Considering that the contour length ($L_C$, 13.6μm[114]) of the T7 genome far exceeds its persistence length ($L_P$, 50 nm[115]), we estimated the mean-square surface-equilibrated end-to-end distance with $L_C \rightarrow \infty$, therefore equation (5.2) becomes

$$\langle R^2 \rangle_{2D} = 4L_P L_C \tag{5.3}$$

Following the same consideration, the mean-square projected end-to-end distance can then be calculated as[113]

$$\langle R^2 \rangle_{proj} = \frac{1}{3} \langle R^2 \rangle_{2D} \tag{5.4}$$

Given the above parameters of T7 dsDNA, the equilibrated end-to-end distance is expected to be ~1.6 μm and the projected end-to-end distance is ~1.3 μm.

Using these end-to-end distance data, we estimated the size of the area occupied by the surface-adsorbed full-length T7 dsDNA with the following equation, where the radius of gyration ($R_G$) is related to the end-to-end distance ($R$) as

$$\langle R_G^2 \rangle = \frac{\langle R^2 \rangle}{6} \tag{5.5}$$

Accordingly, the diameter of the circular area occupied by the full-length T7 dsDNA is ~1.3 µm and ~0.7 µm for the surface equilibrated and surface-projected conditions, respectively. These values are larger than the measured diameter (355 ±57 nm, SD) of the DNA covered area, which suggests that the ejected and surface-adsorbed DNA was most likely a partial T7 genome in a kinetically trapped structural state.

Furthermore, we often observed regions in the AFM images, in which the ejected DNA threads were parallel with each other, indicating that the molecule was exposed to projectile forces (**Fig. 24.**).

Second, the AFM images also revealed that the DNA ejection occurred via the tail complex (**Fig. 24.b**, **Fig. 25.**) indicating that the process took place forcibly through its natural path. Although the tail complex often maintained its gross conical appearance, it frequently shrunk and sometimes disappeared (**Fig. 24.b**, **Fig. 25.**) pointing at structural rearrangements associated with the ejection process. Furthermore, we excluded the possibility that DNA was ejected due to the cantilever tip breaking off the tail, because even a partial mechanical tapping of the capsid body away from the tail complex resulted in DNA release (**Fig. 37.**).
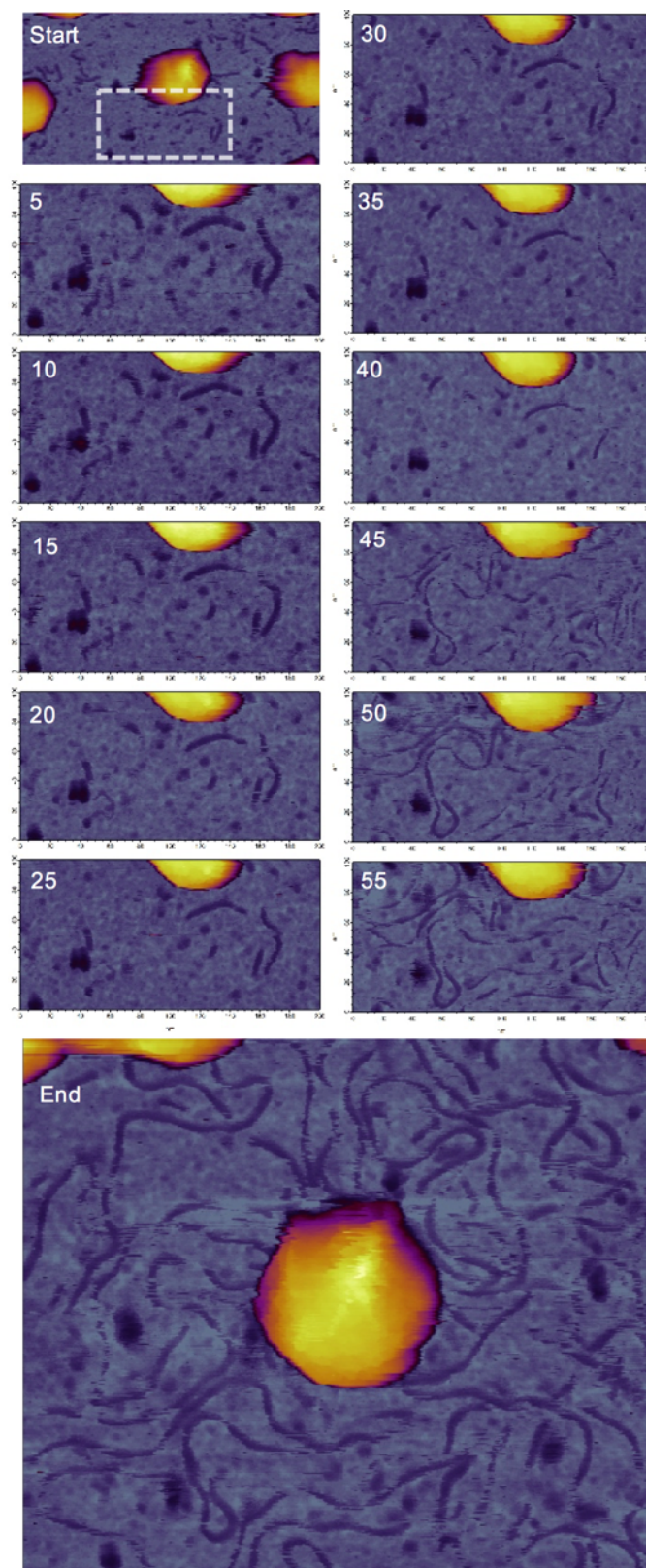
**Fig. 37.** DNA ejection during scanning of bacteriophage T7. Temporal sequence of images separated by 5 minutes are shown. The boxed area in the image labeled "Start" was scanned repetitively with progressively increasing force (lowered setpoint). The bottom image labeled "End" shows the same T7 capsid following the partial tapping experiment.

Third, the DNA appeared on the image within one-line-scan measured at 1 Hz line-scan rate, therefore most of the DNA was ejected in less than 1 s. Considering the 40 kbp genome length, our results are comparable with the rapid 60-75 kbp/s ejection rate measured earlier[116,117], which results in the emission of a significant portion of the viral genome.

Finally, we also found that the mechanical perturbation propagates through the compressible medium of the DNA-filled capsid from the location of the mechanical load towards the tail complex and triggers DNA ejection. Furthermore, the global structure of the capsid remained essentially intact after the DNA ejection and the mechanical perturbation caused neither the collapse of the capsid, nor a gaping hole on its surface.

During the scanning in our measurements, the cantilever oscillated with high frequency (up to 27 kHz) and exerted a given average force on the capsid wall for an extended period of time which might have evoked a signal to trigger the DNA ejection.

We estimated the pressure increment relative to the baseline 60 atm internal pressure of the capsids[118] that was generated due to the cantilever oscillation and led to the DNA ejection.

First, we calibrated each cantilever independently and based on the obtained force versus oscillation amplitude curve (see in **Material and Methods**) we estimated that the capsid was pressed with an average ~40 pN in the instant of the DNA ejection.
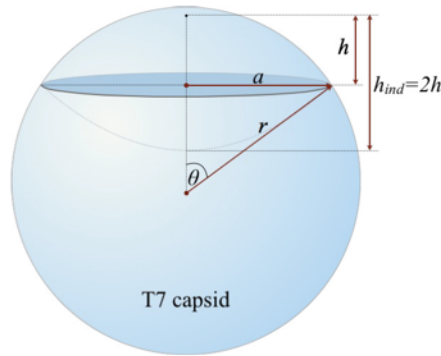


**Fig. 38.** Schematics of T7 indentation with an AFM cantilever as a buckled sphere.

This 40 pN average force caused ~0.057 nm indentation of the capsid based on the previously measured 0.7 N/m capsid stiffness.

$$h_{ind} = \frac{F}{k} \tag{5.6}$$

Indenting the capsid reduces its volume by twice that of the spherical dome (**Fig. 38.b**), which can be calculated from the indentation distance ($h_{ind}=2h$) and the capsid radius (r) as

$$V_\Delta = \frac{2\pi}{3}h^2(3r - h) \tag{5.7}$$

This results in a 0.153 nm³ reduce in the total volume of the spherical capsid, which is $1.13 \times 10^5$ nm³ based on

$$V_C = \frac{4}{3}\pi r^3 \tag{5.8}$$

The pressure increment can then be obtained from compressibility ($\kappa$) as

$$\Delta p = \frac{1}{\kappa}\frac{\Delta V}{V_C} \tag{5.9}$$

which yields a 6.75 - 13.5 kPa (0.067 - 0.133 atm) pressure change given the compressibility range of $1\times10^{-10}$ - $2\times10^{-10}$ 1/Pa measured for globular proteins in water[119].

Consequently, the calculated pressure increment is between 0.1- 0.2% relative to the internal pressure of DNA-filled capsid (60 atm). This may be sufficient to trigger DNA ejection, indicating that the mature T7 phage is on the verge of releasing its genomic material. The persisting force on the capsid wall reduces the lifetime of the pre-ejection structural state of the virus. The force applied by the cantilever in this case was oscillatory, which may contribute to the DNA ejection triggering possibly through causing resonance with the proteins involved in the ejection process.

We speculate that the pre-ejection-state lifetime becomes reduced because the invested mechanical energy lowers the activation barrier towards an initial intermediate state along the DNA ejection pathway. Because the reaction pathway, which likely contains further intermediate states, always ends in the DNA-ejected state, triggering transition is of key importance: once its barrier is crossed, the rest of the transition along the reaction pathway are completed spontaneously.

5.3.2    The Effect of Increased Mechanical Load on the DNA Ejection Triggering Rate

To directly confirm the role of force in triggering DNA-ejection, we scanned the surface attached particles with gradually increasing forces which resulted in more extensive appearance of the ejected DNA. Although the force was applied on the capsid wall, the

ejection occurred via the tail, away from the point of attack. Thus, the mechanical perturbation caused by the cantilever is relayed, as pressure, via the continuum of the capsid wall and the semi-crystalline DNA towards the tail complex. We calculated the ratio of the DNA ejected particles and the cantilever tip residence time on the capsid, from which we estimated the force-dependent DNA-ejection rate ($k_F$). Then we applied the transition state theory to understand the influence of mechanical force ($F$) on the ejection rate.

First, we calculated the total number of capsids ($N_{total}$) in the scanned area and the number of capsids that ejected their DNA as a result of the applied mechanical force ($N_{ejected}$). Then we estimated the average residence time of the cantilever on a capsid ($t_r$) based on the scanning and image parameters. We binary thresholded the AFM image (**Fig. 39.b**) to separate the image pixels of virus particles from the background, which allowed us to estimate the residence time of cantilever interaction with the capsids. Based on the AFM scan rate (0.22 Hz), the number of image pixels per line (512) and considering that the area was scanned twice (forward and backward), one pixel corresponds to 8.9 ms. **Fig. 39.c** shows that the residence time, calculated from the image particle areas, decreases as the loading force increases and is in the order of 1 to 4 seconds.
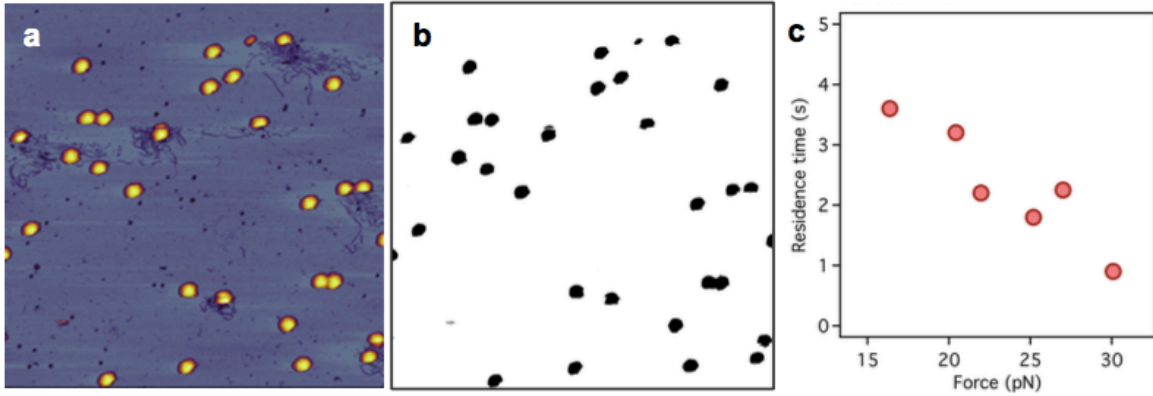


**Fig. 39.** Calculation of the residence time of the cantilever on a capsid. (**a**) Original height-contrast AFM image (**b**) Binary thresholded image of (**a**), (**c**) Residence time as a function of mechanical force.

Based on the residence time, we calculated the force-dependent rate ($k_F$) of DNA ejection according to

$$k_F = \frac{1}{t_r} \frac{N_{ejected}}{N_{total}}$$

(5.10)

Using the previously calculated parameters, we applied the transition-state theory which describes the influence of mechanical force ($F$) on the rate of reactions ($k_F$)[120,121] depending on the invested mechanical energy ($F\Delta x$) relative to the activation energy ($E_a$),

$$k_F = Ae^{-\frac{E_a-F\Delta x}{k_BT}} = Ae^{-\frac{E_a}{k_BT}}e^{\frac{F\Delta x}{k_BT}} = k_0e^{\frac{F\Delta x}{k_BT}} \tag{5.11}$$

where $k_0$ is the rate of the spontaneous process at constant temperature, $\Delta x$ is the distance along the reaction coordinate related to the energetic topology of the system, $k_B$ is the Boltzmann's constant and $T$ is the absolute temperature.

$A$ is the pre-exponential factor which can be expressed by the thermal energy ($k_BT$) and Planck's constant ($h$) as

$$A = \frac{k_BT}{h} \tag{5.12}$$

and was $6\times10^{12}$ 1/s in our experiments at the typical temperature of 20 ˚C.

By fitting equation (5.11) to the $k_F$ *versus* $F$ data points (**Fig. 26.d**), we estimated the value of $k_0$ and $\Delta x$. The $k_0$ spontaneous triggering rate was $2.6\times10^{-5}$ 1/s ($\pm2.7\times10^{-5}$ 1/s). The $\Delta x$ distance between the initial and transition state of the system along the reaction coordinate was 1.2 nm ($\pm0.1$ nm), which corresponds to the expected structural change within the tail related to triggering.

Finally, we calculated the activation energy using the above constants and parameters as

$$E_a = k_BT ln\left(\frac{A}{k_0}\right) \tag{5.13}$$

The resulting activation energy was 23 kcal/mol which compares well with the range of 20-40 kcal/mol found in bulk experiments for the initial steps of viral DNA ejection[98].

The exponential dependence of triggering rate on force acts as a sensitive mechanical switch: below 20-25 pN the rate is negligible but above it triggering rapidly takes place. The triggering rates observed at these forces significantly exceed the lipopolysaccharide-induced tail channel opening rate measured recently for T7[122], suggesting that triggering DNA ejection is indeed extremely sensitive to mechanical force.

In the AFM images, we also observed globular particles in the vicinity of the ejected DNA, which may correspond to the viral core proteins ejected prior to DNA. It is conceivable that

the mechanical energy stored in the encapsulated DNA is utilized both towards the unfolding and ejection of the core proteins and towards the construction and maintenance of the conduit. Such a mechanism might also be relevant in other phages with short, non-contractile tails. Furthermore, the internal pressure likely contributes to mechanically pre-loading the ejection machinery, thereby tilting the energy landscape towards DNA ejection. In this sensitive state, a small additional force is sufficient to trigger the process with an apparently switch-like mechanism.

### 5.3.3  Switch-Like Triggering of the DNA Ejection

To explore the possible mechanisms behind the abrupt triggering of the DNA-ejection, we chemically fixed the surface attached particles with glutaraldehyde prior to scanning them (**Fig. 28.**). The tail fibers of the T7 phages became visible on the capsid surface and, surprisingly, the substrate was already covered with the ejected DNA by the time of scanning. Conceivably, the immobilization of the tail fibers induces a conformational switching that triggers DNA ejection similarly as in the case of mechanical force. Although the details of the conformational switch are yet largely unknown, it might include a lever-like action of the tail fibers that results in a transition within the tail complex.

# 6 CONCLUSIONS

We have shown that exposing the T7 particles to 65 ˚C thermal treatment causes the release of its genomic DNA due to the abruption of the tail complex. The loss of DNA results in a relaxation of the capsid structure accompanied by a reduced stiffness and breaking force. Further heating to 80 ˚C leads to rearrangements within the capsid wall, caused most likely by partial denaturation of the component gp10A proteins. Even though the loss of DNA destabilizes the capsids, they are remarkably capable of withstand high temperatures with a more-or-less intact global topographical structure. Thus, partial denaturation may have a stabilizing effect on the global structural constraints of the viral capsid.

The fatigue experiments revealed that the elastic regime of the nanoindentation force traces contain discrete, stepwise transitions that cause buckling of the T7 capsid with magnitudes that are integer multiples of ~0.6 nm. These transitions are reversible and contribute to the rapid consolidation of the capsid structure against a force during cantilever retraction. The stepwise transitions were present even following the removal of the genomic DNA by heat treatment, indicating that they are related to the structure and dynamics of the capsomeric proteins. Dynamic force spectroscopy experiments showed that the thermally activated consolidation step is ~$10^4$ times faster than spontaneous buckling, suggesting that the capsid stability is under strong dynamic control. Therefore, capsid structural dynamics may play an important role in protecting the genomic material from harsh environmental impacts.

We directly visualized that tapping the capsid wall with an oscillating atomic-force-microscope cantilever triggers rapid DNA ejection via the tail complex. The triggering rate increased exponentially as a function of force, following transition-state theory, across an activation barrier of 23 kcal/mol at 1.2 nm along the reaction coordinate. The conformation of the ejected DNA molecule revealed that it had been exposed to a propulsive force. This force, arising from intra-capsid pressure, assists in initiating the ejection process and the transfer of DNA to outside the capsid wall. The chemical immobilization of the tail fibers also resulted in enhanced DNA ejection, suggesting that the triggering process involves a conformational switch that can be mechanically activated either by external forces or via the tail-fiber complex.

**Novel scientific results:**

I.  Exposing the T7 capsids to a thermal treatment at 65 ˚C causes the release of their DNA due to the abruption of the tail complex, which leads to the relaxation of the capsid structure. Further heating to 80 ˚C results in increased mechanical stability due to partial denaturation of the capsomeric proteins kept within the global capsid arrangement.

II. The elastic regime of the nanoindentation force traces contains discrete, stepwise transitions which may be related to the buckling of the pentamers. These transitions are reversible and contribute to the rapid consolidation of the capsid structure against force during cantilever retraction. The capsid stability is under dynamic control, and in thermal equilibrium the reaction is strongly biased towards the intact structural state.

III. Tapping the capsid wall with an oscillating AFM cantilever triggers rapid DNA ejection via the tail complex. The triggering rate increases exponentially as a function of force, following transition-state theory. The triggering process might involve a conformational switch that can be activated by mechanical force.

# 7  SUMMARY

Viruses are infectious obligate intracellular parasites that comprise a nanometer-sized protein capsid and an internal genome. The capsid protects the genome from exposure to deleterious chemical and physical effects in the extracellular environment and, in DNA viruses, it also harbors the machinery for the efficient packaging and infectious exposition of the genomic material.

We performed topographical and indentation experiments on T7 bacteriophage with AFM to explore their nanomechanical properties and force-induced structural changes in various environmental condition.

We found that exposure to 65 ˚C causes the release of genomic DNA due to the loss of the capsid tail which consequently leads to a destabilization of the T7 particles. Further heating to 80 ˚C surprisingly increases the mechanical stability through partial denaturation of the capsomeric proteins kept within the global capsid arrangement.

The elastic regime of the nanoindentation force traces contain discrete, stepwise transitions that cause buckling of the T7 capsid. We showed that these transitions are reversible, related to the capsid proteins and contribute to the rapid consolidation of the capsid structure. Our dynamic force "spectroscopy" experiments revealed that the thermally activated consolidation step is $\sim 10^4$ times faster than spontaneous buckling, suggesting that the capsid stability is under strong dynamic control.

In situ experiments allowed a direct visualization of the dsDNA ejection from a viral capsid upon mechanical trigger. We found that with increasing mechanical load, the rate of triggering DNA-ejection increases exponentially according to the transition-state theory. Furthermore, the forces required to trigger DNA ejection cause negligibly small changes in the internal pressure of the capsid. Thus, we concluded that the DNA-filled capsid is in a state poised for expelling its genomic material and the proteins needed for the faithful execution of the initial steps of phage infection. Finally, our results also indicate that DNA ejection is controlled by a sensitive conformational switch that can be activated by mechanical force.

# 8 ÖSSZEFOGLALÁS

A vírusok fertőző obligát intracelluláris paraziták, melyeket egy nanométeres nagyságrendű fehérje kapszid és a benne foglalt örökítőanyag épít fel. A kapszid feladata, hogy megvédje az örökítőanyagot a külső káros kémiai és fizikai hatásoktól, továbbá DNS vírusok esetén egyaránt felel az örökítő anyag továbbításáért: a kapszidba csomagolásért és a gazdaszervezetbe juttatásért.

AFM segítségével topográfiai és indentációs kísérleteket végeztünk T7 bakteriofágokon annak érdekében, hogy feltérképezzük nanomechanikai tulajdonságaikat és a különböző környezeti feltételek mellett végbemenő, a ráható erő-által kiváltott strukturális változásaikat.

Eredményeink azt mutatják, hogy a 65 ˚C-os hőkezelés hatására a DNS kiszabadul a kapszidból a farok régió elvesztése miatt, ami végül a T7 partikulumok destabilizálódásához vezet. A hőmérséklet további 80 ˚C-ra történő emelése, meglepően a kapszidok mechanikai stabilitásának növekedéséhez vezetett a kapszomer fehérjék részleges denaturációjának következtében, a globális szerkezeti struktúrát megtartva.

A nanoindentációs erő-görbék rugalmas tartománya diszkrét, lépcsőszerű átmeneteket tartalmaz, amelyek a kapszid horpadásaihoz (buckling) köthetők. Az átmenetek reverzibilisek, a kapszid fehérjékkel kapcsolatosak és hozzájárulnak a kapszid gyors szerkezeti visszaalakulásához. A dinamikus erőspektroszkópiai méréseink megmutatták, hogy a termikusan aktivált visszaalakulás mintegy $10^4$-szer gyorsabban megy végbe mint a spontán horpadás. Ez arra utal, hogy a kapszid stabilitása erős dinamikus kontroll alatt áll.

In situ kísérleteink lehetővé tették a mechanikailag indukált DNS kiszabadulás közvetlen megjelenítését. Azt találtuk, hogy a mechanikai terhelés növelése, az átmenetiállapot-elméletnek megfelelően exponenciálisan növelte az indukált DNS kiszabadulás sebességét. Továbbá a DNS kiszabadulás előidézéséhez szükséges erő elhanyagolhatóan alacsony változást okoz a kapszid belső nyomásában. Így arra a következtetésre jutottunk, hogy a kapszidba zárt DNS a kiszabadulás határán van és a fertőzés megkezdéséhez mindössze néhány fehérje konformációváltozása szükséges. Végül eredményeink azt is megmutatták, hogy a DNS kiszabadulását egy érzékeny konformációtól függő kapcsoló irányítja, amely mechanikai erő által is aktiválható.

# 9    LIST OF PUBLICATIONS

## 9.1    Publications related to the dissertation

Vörös Z, Csík G, Herényi L, Kellermayer MSZ. (2017) Stepwise reversible nanomechanical buckling in a viral capsid. *Nanoscale,* **9:** 1136–1143.

Kellermayer MSZ, Vörös Z, Csík G, Herényi L. (2018) Forced phage uncorking: viral DNA ejection triggered by a mechanically sensitive switch. *Nanoscale,* **10:** 1898–1904.

Vörös Z, Csík G, Herényi L, Kellermayer MSZ. Temperature-dependent nanomechanics and topography of bacteriophage T7. *Under review*

## 9.2    Publications unrelated to the dissertation

Vörös Z, Yan Y, Kovari DT, Finzi L, Dunlap D. (2017) Proteins mediating DNA loops effectively block transcription. *Protein Sci.,* **26:** 1427–1438.

Reinemann DN, Sturgill EG, Das DK, Degen MS, Vörös Z, Hwang W, Ohi R, Lang MJ. (2017) Collective Force Regulation in Anti-parallel Microtubule Gliding by Dimeric Kif15 Kinesin Motors. *Curr. Biol.,* **27:** 2810–2820.

## 10  BIBLIOGRAPHY

1.  Venkataram Prasad BV, Schmid MF. (2012) Principles of Virus Structural Organization. *Adv Exp Med Biol.*, **726**: 17–47.

2.  Flint SJ, Enquist LW, Racaniello VR, Skalka AM, Barnum DR. (2004) *Principles of virology: Molecular biology, pathogenesis, and control of animal viruses.*, ASM Press, Washington, D.C, 59-65pp.

3.  Caspar DL, Klug A. (1962) Physical principles in the construction of regular viruses. *Cold Spring Harb. Symp. Quant. Biol.*, **27**: 1–24.

4.  Mateu MG. (2013) *Structure and physics of viruses.*, Sringer, London, 53-75pp.

5.  Hulo C, De Castro E, Masson P, Bougueleret L, Bairoch A, Xenarios I, Le Mercier P. (2011) ViralZone: A knowledge resource to understand virus diversity. *Nucleic Acids Res.*, **39**: 576–582.

6.  Tóth K, Rontó G. (1987) Salt Effects on Bacteriophage T7-I. *Physiol. Chem. Phys. Med. NMR*, **19**: 59–66.

7.  Tóth K, Csík G, Rontó G. (1987) Salt effects on the bacteriophage T7-II structure and activity changes. *Physiol. Chem. Phys. Med. NMR*, **19**: 67–74.

8.  Csík G, Egyeki M, Herényi L, Majer Z, Tóth K. (2009) Role of structure-proteins in the porphyrin – DNA interaction. *J. Photochem. Photobiol. B Biol.*, **96**: 207–215.

9.  Zupán K, Herényi L, Tóth K, Majer Z, Csík G. (2004) Binding of Cationic Porphyrin to Isolated and Encapsidated Viral DNA Analyzed by Comprehensive Spectroscopic Methods. *Biochemistry*, **43**: 9151–9159.

10. Rontó G, Tóth K, Csík G, Feigin LA, Svergun DT, Dembo AT, E.V. S. (1988) Loosening of the phage structure in low ionic strength encironement. *Eur. Biophys. J.*, **15**: 293–298.

11. Rontó G, Agamalyan MM, Drabkin GM, Feigin LA, Lvov YM. (1983) Structure of bacteriophage T7. Small-angle X-ray and neutron scattering study. *Biophys. J.*, **43**: 309–314.

12. Ionel A, Velázquez-Muriel J, Luque D, Cuervo A, Castón JR, Valpuesta JM, Martín-Benito J, Carrascosa JL. (2011) Molecular rearrangements involved in the capsid

shell maturation of bacteriophage T7. *J. Biol. Chem.*, **286**: 234–42.

13. Agirrezabala X, Martín-Benito J, Valle M, González JM, Valencia A, Valpuesta JM, Carrascosa JL. (2005) Structure of the connector of bacteriophage T7 at 8A resolution: structural homologies of a basic component of a DNA translocating machinery. *J. Mol. Biol.*, **347**: 895–902.

14. Cerritelli ME, Trus BL, Smith CS, Cheng N, Conway JF, Steven AC. (2003) A Second Symmetry Mismatch at the Portal Vertex of Bacteriophage T7: 8-fold Symmetry in the Procapsid Core. *J. Mol. Biol.*, **327**: 1–6.

15. Berman HM, Westbrook J, Feng Z, Gilliland G, Bhat TN, Weissig H, Shindyalov IN, Bourne PE. (2000) The protein data bank. *Nucleic Acids Res.*, **28**: 235–242.

16. Rose AS, Hildebrand PW. (2015) NGL Viewer: A web application for molecular visualization. *Nucleic Acids Res.*, **43**: W576–W579.

17. Agirrezabala X, Martín-Benito J, Castón JR, Miranda R, Valpuesta JM, Carrascosa JL. (2005) Maturation of phage T7 involves structural modification of both shell and inner core components. *EMBO J.*, **24**: 3820–9.

18. Guo F, Liu Z, Fang P-A, Zhang Q, Wright ET, Wu W, Zhang C, Vago F, Ren Y, Jakana J, Chiu W, Serwer P, Jiang W. (2014) Capsid expansion mechanism of bacteriophage T7 revealed by multistate atomic models derived from cryo-EM reconstructions. *Proc. Natl. Acad. Sci.*, **111**: E4606–E4614.

19. Binnig G, Quate CF. (1986) Atomic Force Microscope. *Phys. Rev. Lett.*, **56**: 930–933.

20. Binnig G, Rohrer H. (1983) Scanning tunneling microscopy. *Surf. Sci.*, **126**: 236–244.

21. Gibson CT, Watson GS, Myhra S. (1999) Determination of the spring constants of probes for force microscopy/spectroscopy. *Nanotechnology*, **7**: 259–262.

22. Cleveland JP, Manne S, Bocek D, Hansma PK. (1993) A nondestructive method for determining the spring constant of cantilevers for scanning force microscopy. *Rev. Sci. Instrum.*, **64**: 403–405.

23. Sader JE, Chon JWM, Mulvaney P. (1999) Calibration of rectangular atomic force microscope cantilevers. *Rev. Sci. Instrum.*, **70**: 3967.

24. Hutter JL, Bechhoefer J. (1993) Calibration of atomic-force microscope tips. *Rev. Sci. Instrum.*, **64**: 1868–1873.

25. Canale C, Torre B, Ricci D, Braga PC. (2011) *Atomic Force Microscopy in Biomedical Research - Book. Methods Mol. Biol.*, **736**, 31-43pp.

26. Carrillo PJP, Medrano M, Valbuena A, Rodríguez-Huete A, Castellanos M, Pérez R, Mateu MG. (2017) Amino Acid Side Chains Buried along Intersubunit Interfaces in a Viral Capsid Preserve Low Mechanical Stiffness Associated with Virus Infectivity. *ACS Nano*, **11**: 2194–2208.

27. Ikai, Atsushi, Kousei Yoshimura, Fumio Arisaka, Akishige Ritani and KI. (1993) Atomic force microscopy of bacteriophage T4 and its tube-baseplate complex. *FEBS Lett.*, **326**: 39–41.

28. Lyubchenko YL, Oden PI, Lampner D, Lindsay SM, Dunker KA. (1993) Atomic force microscopy of DNA and bacteriophage in air, water and propanol: The role of adhesion forces. *Nucleic Acids Res.*, **21**: 1117–1123.

29. Ohnesorge FM, Hörber JK, Häberle W, Czerny CP, Smith DP, Binnig G. (1997) AFM review study on pox viruses and living cells. *Biophys. J.*, **73**: 2183–94.

30. Kuznetsov YG, Malkin AJ, Lucas RW, Plomp M, McPherson A. (2001) Imaging of viruses by atomic force microscopy. *J. Gen. Virol.*, **82**: 2025–2034.

31. Malkin, A. J., Yu G. Kuznetsov and AM. (2001) Viral capsomere structure, surface processes and growth kinetics in the crystallization of macromolecular crystals visualized by in situ atomic force microscopy. *J. Cryst. Growth*, **232**: 173–183.

32. Plomp M, Rice MK, Wagner EK, Mcpherson A, Malkin AJ. (2002) Rapid Visualization at High Resolution of Pathogens by Atomic Force Microscopy. *Amer. J. Pathol.*, **160**: 1959–1966.

33. Kuznetsov YG, Low A, Fan H, McPherson A. (2004) Atomic force microscopy investigation of wild-type Moloney murine leukemia virus particles and virus particles lacking the envelope protein. *Virology*, **323**: 189–96.

34. Kuznetsov YG, Gurnon JR, Van Etten JL, McPherson A. (2005) Atomic force microscopy investigation of a chlorella virus, PBCV-1. *J. Struct. Biol.*, **149**: 256–263.

35. Kuznetsov YG, Martiny JBH, McPherson A. (2010) Structural analysis of a Synechococcus myovirus S-CAM4 and infected cells by atomic force microscopy. *J. Gen. Virol.*, **91**: 3095–104.

36. Giocondi M-C, Ronzon F, Nicolai MC, Dosset P, Milhiet P-E, Chevalier M, Le Grimellec C. (2010) Organization of influenza A virus envelope at neutral and low pH. *J. Gen. Virol.*, **91**: 329–38.

37. Kuznetsov YG, Xiao C, Sun S, Raoult D, Rossmann M, McPherson A. (2010) Atomic force microscopy investigation of the giant mimivirus. *Virology*, **404**: 127–137.

38. Kuznetsov YG, Chang S-C, McPherson A. (2011) Investigation of bacteriophage T4 by atomic force microscopy. *Bacteriophage*, **1**: 165–173.

39. Martinez-Martin D, Carrasco C, Hernando-Perez M, de Pablo PJ, Gomez-Herrero J, Perez R, Mateu MG, Carrascosa JL, Kiracofe D, Melcher J, Raman A. (2012) Resolving structure and mechanical properties at the nanoscale of viruses with frequency modulation atomic force microscopy. *PLoS One*, **7**: e30204.

40. Zhao Q, Allen MJ, Wang Y, Wang B, Wang N, Shi L, Sitrin RD. (2012) Disassembly and reassembly improves morphology and thermal stability of human papillomavirus type 16 virus-like particles. *Nanomedicine*, **8**: 1182–9.

41. Kuznetsov YG, Klose T, Rossmann M, McPherson A. (2013) Morphogenesis of mimivirus and its viral factories: an atomic force microscopy study of infected cells. *J. Virol.*, **87**: 11200–11213.

42. Meyring-Wösten A, Hafezi W, Kühn J, Liashkovich I, Shahin V. (2014) Nano-visualization of viral DNA breaching the nucleocytoplasmic barrier. *J. Control. Release*, **173**: 96–101.

43. Tiwari PM, Eroglu E, Boyoglu-Barnum S, He Q, Willing G a, Vig K, Dennis V a, Singh SR. (2014) Atomic force microscopic investigation of respiratory syncytial virus infection in HEp-2 cells. *J. Microsc.*, **253**: 31–41.

44. Hernando-Pérez M, Pascual E, Aznar M, Ionel A, Castón JR, Luque A, Carrascosa JL, Reguera D, de Pablo PJ. (2014) The interplay between mechanics and stability of viral cages. *Nanoscale*, **6**: 2702–9.

45. Valbuena A, Mateu MG. (2015) Quantification and modification of the equilibrium dynamics and mechanics of a viral capsid lattice self-assembled as a protein nanocoating. *Nanoscale*, **7**: 14953–14964.

46. Hernando-Pérez M, Cartagena-Rivera AX, Lošdorfer Božič A, Carrillo PJP, San Martín C, Mateu MG, Raman A, Podgornik R, de Pablo PJ. (2015) Quantitative nanoscale electrostatics of viruses. *Nanoscale*, **7**: 17289–17298.

47. Medrano M, Fuertes MÁ, Valbuena A, Carrillo PJP, Rodríguez-Huete A, Mateu MG. (2016) Imaging and Quantitation of a Succession of Transient Intermediates Reveal the Reversible Self-Assembly Pathway of a Simple Icosahedral Virus Capsid. *J. Am. Chem. Soc.*, **138**: 15385–15396.

48. Falvo MR, Washburn S, Superfine R, Finch M, Brooks FP, Chi V, Taylor RM. (1997) Manipulation of individual viruses: friction and mechanical properties. *Biophys. J.*, **72**: 1396–1403.

49. Ivanovska IL, de Pablo PJ, Ibarra B, Sgalari G, MacKintosh FC, Carrascosa JL, Schmidt CF, Wuite GJL. (2004) Bacteriophage capsids: tough nanoshells with complex elastic properties. *Proc. Natl. Acad. Sci. U. S. A.*, **101**: 7600–5.

50. Kol N, Gladnikoff M, Barlam D, Shneck RZ, Rein A, Rousso I. (2006) Mechanical properties of murine leukemia virus particles: effect of maturation. *Biophys. J.*, **91**: 767–74.

51. Carrasco C, Carreira a, Schaap I a T, Serena P a, Gómez-Herrero J, Mateu MG, de Pablo PJ. (2006) DNA-mediated anisotropic mechanical reinforcement of a virus. *Proc. Natl. Acad. Sci. U. S. A.*, **103**: 13706–13711.

52. Michel JP, Ivanovska IL, Gibbons MM, Klug WS, Knobler CM, Wuite GJL, Schmidt CF. (2006) Nanoindentation studies of full and empty viral capsids and the effects of capsid protein mutations on elasticity and strength. *Proc. Natl. Acad. Sci. U. S. A.*, **103**: 6184–6189.

53. Roos WH, Ivanovska IL, Evilevitch a, Wuite GJL. (2007) Viral capsids: mechanical characteristics, genome packaging and delivery mechanisms. *Cell. Mol. Life Sci.*, **64**: 1484–97.

54. Kol N, Shi Y, Tsvitov M, Barlam D, Shneck RZ, Kay MS, Rousso I. (2007) A stiffness switch in human immunodeficiency virus. *Biophys. J.*, **92**: 1777–83.

55.     Ivanovska I, Wuite G, Jönsson B, Evilevitch A. (2007) Internal DNA pressure modifies stability of WT phage. *Proc. Natl. Acad. Sci. U. S. A.*, **104**: 9603–8.

56.     Carrasco C, Castellanos M, de Pablo PJ, Mateu MG. (2008) Manipulation of the mechanical properties of a virus by protein engineering. *Proc. Natl. Acad. Sci. U. S. A.*, **105**: 4150–5.

57.     Roos WH, Radtke K, Kniesmeijer E, Geertsema H, Sodeik B, Wuite GJL. (2009) Scaffold expulsion and genome packaging trigger stabilization of herpes simplex virus capsids. *Proc. Natl. Acad. Sci. U. S. A.*, **106**: 9673–8.

58.     Roos WH, Bruinsma R, Wuite GJL. (2010) Physical virology. *Nat. Phys.*, **6**: 733–743.

59.     Carrasco C, Luque a, Hernando-Pérez M, Miranda R, Carrascosa JL, Serena P a, de Ridder M, Raman a, Gómez-Herrero J, Schaap I a T, Reguera D, de Pablo PJ. (2011) Built-in mechanical stress in viral shells. *Biophys. J.*, **100**: 1100–8.

60.     Ivanovska IL, Miranda R, Carrascosa JL, Wuite GJL, Schmidt CF. (2011) Discrete fracture patterns of virus shells reveal mechanical building blocks. *Proc. Natl. Acad. Sci. U. S. A.*, **108**: 12611–6.

61.     Baclayon M, Shoemaker GK, Uetrecht C, Crawford SE, Estes MK, Prasad BVV, Heck AJR, Wuite GJL, Roos WH. (2011) Prestress Strengthens the Shell of Norwalk Virus Nanoparticles. *Nano Lett.*, **11**: 4865–4869.

62.     Castellanos M, Pérez R, Carrasco C, Hernando-Pérez M, Gómez-Herrero J, de Pablo PJ, Mateu MG. (2012) Mechanical elasticity as a physical signature of conformational dynamics in a virus particle. *Proc. Natl. Acad. Sci. U. S. A.*, **109**: 12028–33.

63.     Mateu MG. (2012) Mechanical properties of viruses analyzed by atomic force microscopy: a virological perspective. *Virus Res.*, **168**: 1–22.

64.     Kurland NE, Drira Z, Yadavalli VK. (2012) Measurement of nanomechanical properties of biomolecules using atomic force microscopy. *Micron*, **43**: 116–28.

65.     Castellanos M, Pérez R, Carrillo PJP, de Pablo PJ, Mateu MG. (2012) Mechanical disassembly of single virus particles reveals kinetic intermediates predicted by theory. *Biophys. J.*, **102**: 2615–24.

66. Roos W, Gertsman I. (2012) Mechanics of bacteriophage maturation. *Proc. Natl. Acad. Sci. U. S. A.*, **109**: 2342–2347.

67. Snijder J, Ivanovska IL, Baclayon M, Roos WH, Wuite GJL. (2012) Probing the impact of loading rate on the mechanical properties of viral nanoparticles. *Micron*, **43**: 1343–50.

68. Ortega-Esteban A, Pérez-Berná a J, Menéndez-Conejero R, Flint SJ, San Martín C, de Pablo PJ. (2013) Monitoring dynamics of human adenovirus disassembly induced by mechanical fatigue. *Sci. Rep.*, **3**: 1434.

69. Snijder J, Reddy VS, May ER, Roos WH, Nemerow GR, Wuite GJL. (2013) Integrin and defensin modulate the mechanical properties of adenovirus. *J. Virol.*, **87**: 2756–66.

70. Kononova O, Snijder J, Brasch M, Cornelissen J, Dima RI, Marx K a, Wuite GJL, Roos WH, Barsegov V. (2013) Structural transitions and energy landscape for Cowpea Chlorotic Mottle Virus capsid mechanics from nanomanipulation in vitro and in silico. *Biophys. J.*, **105**: 1893–903.

71. Hernando-Pérez, M., Lambert, S., Nakatani-Webster, E., Catalano, C. E., & De Pablo PJ. (2014) Cementing proteins provide extra mechanical stabilization to viral cages. *Nat. Commun.*, **5**: 4520.

72. Castellanos M, Carrillo PJP, Mateu MG. (2015) Quantitatively probing propensity for structural transitions in engineered virus nanoparticles by single-molecule mechanical analysis. *Nanoscale*, **7**: 5654–5664.

73. Coppari E, Imperatori F, Bizzarri AR, Casto R, Santi L, Llauro A, Cannistraro S, Pablo PJ De. (2015) Article Calcium Ions Modulate the Mechanics of Tomato Bushy Stunt Virus. *Biophys. J.*, **109**: 390–397.

74. Pablo PJ De, Schaap IAT. (2015) Fluorescence Tracking of Genome Release during Mechanical Unpacking of Single Viruses,: 10571–10579doi:10.1021/acsnano.5b03020.

75. Mertens J, Casado S, Mata CP, Hernando-pérez M, Pablo PJ De, Carrascosa JL, Castón JR. (2015) A protein with simultaneous capsid scaffolding and dsRNA-binding activities enhances the birnavirus capsid mechanical stability. *Nat. Publ. Gr.*,: 1–11doi:10.1038/srep13486.

76.    Chillo M, Flint SJ, Ortega-esteban A, Condezo GN, Pe AJ, Reguera D, Martı CS. (2015) Mechanics of Viral Chromatin Reveals the Pressurization of Human Adenovirus. *ACS Nano*, **9**: 10826–10833.

77.    Marchetti M, Wuite G, Roos W. (2016) Atomic force microscopy observation and characterization of single virions and virus-like particles by nano-indentation. *Curr. Opin. Virol.*, **18**: 82–88.

78.    Ramalho R, Rankovic S, Zhou J, Aiken C, Rousso I. (2016) Analysis of the mechanical properties of wild type and hyperstable mutants of the HIV - 1 capsid. *Retrovirology*, **13**: 17.

79.    Guerra P, Valbuena A, Querol-Audí J, Silva C, Castellanos M, Rodríguez-Huete A, Garriga D, Mateu MG, Verdaguer N. (2017) Structural basis for biologically relevant mechanical stiffening of a virus capsid by cavity-creating or spacefilling mutations. *Sci. Rep.*, **7**: 4101.

80.    Bittner AM, Alonso JM, Gorzny MŁ, Wege C. (2013) *Nanoscale Science and Technology with Plant Viruses and Bacteriophages*, **68**.

81.    Douglas T. (2006) Viruses: Making Friends with Old Foes. *Science (80-. ).*, **312**: 873–875.

82.    Kim KT, Meeuwissen SA, Nolte RJM, van Hest JCM. (2010) Smart nanocontainers and nanoreactors. *Nanoscale*, **2**: 844.

83.    Mateu MG. (2011) Virus engineering: Functionalization and stabilization. *Protein Eng. Des. Sel.*, **24**: 53–63.

84.    Wen AM, Rambhia PH, French RH, Steinmetz NF. (2013) Design rules for nanomedical engineering: From physical virology to the applications of virus-based materials in medicine. *J. Biol. Phys.*, **39**: 301–325.

85.    Yildiz I, Shukla S, Steinmetz NF. (2011) Applications of viral nanoparticles in medicine. *Curr. Opin. Biotechnol.*, **22**: 901–908.

86.    Strauss JHJ, Sinsheimer RL. (1963) Purification and Properties of Bacteriophage MS2 and of its Ribonucleic Acid. *J. Mol. Biol.*, **7**: 43–54.

87.    Wang H, Bash R, Yodh JG, Hager GL, Lohr D, Lindsay SM. (2002) Glutaraldehyde modified mica: a new surface for atomic force microscopy of chromatin. *Biophys. J.*,

**83**: 3619–25.

88. Foster RA, Johnson FH, Miller VK. (1949) The influence of hydrostatic pressure and urethane on the thermal inactivation of bacteriophage. *J. Gen. Physiol.*, **33**: 1–16.

89. Pollard EC, Solosko W. (1971) The thermal inactivation of T4 and λ bacteriophage. *Biophys. J.*, **11**: 66–74.

90. Yamagishi H, Ozeki H. (1972) Comparative study of thermal inactivation of phage φ80 and lambda. *Virology*, **48**: 316–322.

91. Wetzel R, Perry LJ, Baaset WA, Becktelt WJ. (1988) Disulfide bonds and thermal stability in T4 lysozyme. *Proc. Natl. Acad. Sci.*, **85**: 401–405.

92. Conway JF, Cheng N, Ross PD, Hendrix RW, Duda RL, Steven AC. (2007) A thermally induced phase transition in a viral capsid transforms the hexamers , leaving the pentamers unchanged, **158**: 224–232.

93. Duda RL, Ross PD, Cheng N, Firek BA, Hendrix RW, Conway JF, Steven AC. (2009) Structure and Energetics of Encapsidated DNA in Bacteriophage HK97 Studied by Scanning Calorimetry and Cryo-electron Microscopy. *J. Mol. Biol.*, **391**: 471–483.

94. Qiu X. (2012) Heat Induced Capsid Disassembly and DNA Release of Bacteriophage λ. *PLoS One*, **7**: e39793.

95. Molineux IJ. (2001) No syringes please, ejection of phage T7 DNA from the virion is enzyme driven. *Mol. Microbiol.*, **40**: 1–8.

96. Kemp P, Gupta M, Molineux IJ. (2004) Bacteriophage T7 DNA ejection into cells is initiated by an enzyme-like mechanism. *Mol. Microbiol.*, **53**: 1251–1265.

97. Hu B, Margolin W, Molineux IJ, Liu J. (2013) The bacteriophage t7 virion undergoes extensive structural remodeling during infection. *Science (80-. ).*, **339**: 576–579.

98. Molineux IJ, Panja D. (2013) Popping the cork: mechanisms of phage genome ejection. *Nat. Rev. Microbiol.*, **11**: 194–204.

99. Molineux IJ. (2006) Fifty-three years since Hershey and Chase; Much ado about pressure but which pressure is it? *Virology*, **344**: 221–229.

100. Bianco P, Nagy A, Kengyel A, Szatmári D, Mártonfalvi Z, Huber T, Kellermayer MSZ. (2007) Interaction forces between F-actin and titin PEVK domain measured

with optical tweezers. *Biophys. J.*, **93**: 2102–2109.

101. Munday JN, Capasso F, Parsegian VA, Bezrukov SM. (2008) Measurements of the Casimir-Lifshitz force in fluids: the effect of electrostatic forces and Debye screening. *Phys. Rev. A*, **78**: 32109.

102. Datta SS, Kim S-H, Paulose J, Abbaspourrad A, Nelson DR, Weitz DA. (2012) Delayed Buckling and Guided Folding of Inhomogeneous Capsules. *Phys. Rev. Lett.*,: 109(13), 134302.doi:10.1103/PhysRevLett.109.134302.

103. Knoche S, Kierfeld J. (2011) Buckling of spherical capsules. *Phys. Rev. E - Stat. Nonlinear, Soft Matter Phys.*, **84**.

104. Lidmar J, Mirny L, Nelson DR. (2003) Virus shapes and buckling transitions in spherical shells. *Phys. Rev. E. Stat. Nonlin. Soft Matter Phys.*, **68**: 51910.

105. Mannige R V, Brooks CL. (2009) Geometric considerations in virus capsid size specificity, auxiliary requirements, and buckling. *Proc. Natl. Acad. Sci.*, **106**: 8531–8536.

106. May ER, Brooks CL. (2012) On the Morphology of Viral Capsids: Elastic Properties and Buckling Transitions. *J. Phys. Chem. B*, **116**: 8604–8609.

107. Paulose J, Nelson DR. (2013) Buckling pathways in spherical shells with soft spots. *Soft Matter*, **9**: 8227.

108. Vaziri A, Mahadevan L. (2008) Localized and extended deformations of elastic shells. *Proc. Natl. Acad. Sci. U. S. A.*, **105**: 7913–7918.

109. Vliegenthart GA, Gompper G. (2006) Mechanical deformation of spherical viruses with icosahedral symmetry. *Biophys. J.*, **91**: 834–41.

110. Zandi R, Reguera D. (2005) Mechanical properties of viral capsids. *Phys. Rev. E*, **72**: 21917.

111. Jarzynski C. (1997) Equilibrium free energy differences from nonequilibrium measurements: a master equation approach. *Phys. Rev. E*, **56**: 5018.

112. Ross PD, Conway JF, Cheng N, Dierkes L, Firek BA, Hendrix RW, Steven AC, Duda RL. (2006) A Free Energy Cascade with Locks Drives Assembly and Maturation of Bacteriophage HK97 Capsid. *J. Mol. Biol.*, **364**: 512–525.

113. Rivetti C, Guthold M, Bustamante C. (1996) Scanning Force Microscopy of DNA

Deposited onto Mica: Equilibration versus Kinetic Trapping Studied by Statistical Polymer Chain Analysis. *J. Mol. Biol.*, **264**: 919–932.

114. Cerritelli ME, Cheng N, Rosenberg AH, McPherson CE, Booy FP, Steven AC. (1997) Encapsidated conformation of bacteriophage T7 DNA. *Cell*, **91**: 271–80.

115. Smith SB, Cui Y, Bustamante C, Smith SB, Cui Y, Bustamante C. (2013) B-DNA : The Elastic Response of Overstretching Individual Double-Stranded and Single-Stranded, **271**: 795–799.

116. Grayson P, Han L, Winther T, Phillips R. (2007) Real-time observations of single bacteriophage lambda DNA ejections in vitro. *Proc. Natl. Acad. Sci. U. S. A.*, **104**: 14652–14657.

117. Mangenot S, Hochrein M, Rädler J, Letellier L. (2005) Real-Time Imaging of DNA Ejection from Single Phage Particles. *Curr. Biol.*, **15**: 430–435.

118. Smith DE, Tans SJ, Smith SB, Grimes S, Anderson DL, Bustamante C. (2001) The bacteriophage phi 29 portal motor can package DNA against a large internal force. *Nature*, **413**: 748–752.

119. Kharakoz DP. (2000) Protein Compressibility , Dynamics , and Pressure. *Biophys. J.*, **79**: 511–525.

120. Bell GI. (1978) Models for the specific adhesion of cells to cells. *Science (80-. ).*, **200**: 618–27.

121. Evans E, Ritchie K. (1997) Dynamic strength of molecular adhesion bonds. *Biophys. J.*, **72**: 1541–55.

122. González-García VA, Pulido-Cid M, Garcia-Doval C, Bocanegra R, Van Raaij MJ, Martín-Benito J, Cuervo A, Carrascosa JL. (2015) Conformational changes leading to T7 DNA delivery upon interaction with the bacterial receptor. *J. Biol. Chem.*, **290**: 10038–10044.

## 11 KÖSZÖNETNYILVÁNÍTÁS (ACKNOWLEDGMENT)

Köszönetemet szeretném kifejezni témavezetőmnek, Dr. Kellermayer Miklósnak, a kiváló szakmai útmutatásáért, tanácsaiért és áldozatos munkájáért. Hálával tartozom, amiért nyugodt és biztos kutatási feltételeket biztosított, valamint rugalmasan támogatta a szakmai gyakorlatok iránti érdeklődésemet.

Köszönet illeti Dr. Csík Gabriellát és Dr. Herényi Leventét a kutatói munkámban nyújtott aktív segítségéért. Építő kritikájuk és értékes tanácsaik jelentősen hozzájárultak az eredményeim értelmezéséhez.

Köszönetemet szeretném kifejezni Dr. Murvai Csilla Ünigének, amiért bevezetett a kutatás és az atomerőmikroszkópia alapjaiba, valamint Dr. Bozó Tamásnak az értékes tanácsaiért és ötleteiért.

Köszönet illeti a Biofizika Intézet összes dolgozóját, akik kérdéseimre mindig készségesen és türelmesen válaszoltak és érdeklődéssel követték a munkámat.

Külön köszönetemet és hálámat szeretném kifejezni családomnak, szüleimnek és bátyámnak, akik minden helyzetben nyitottsággal és töretlen bizalommal támogattak. Nem utolsó sorban hálás köszönetemet fejezem ki férjemnek a végtelen türelméért, biztatásáért és szerkesztői munkájáért egyaránt.